Geophys. J. R. astr. Soc. (1975) **42**, 217–250.

Temperature Dependence of Single-Crystal Spinel ($MgAl_2O_4$) Elastic Constants from 293 to 423°K Measured by Light-Sound Scattering in the Raman-Nath Region

Hsi-Ping Liu, R. N. Schock and Don L. Anderson

(Received 1974 September 20)

Summary

The temperature dependence of single-crystal elastic constants of synthetic stoichiometric $MgAl_2O_4$ spinel has been measured by the light-sound scattering technique in the Raman–Nath region. The crystal is set into forced vibration by a single crystal $LiNbO_3$ transducer coupled to one crystal face. A He–Ne Laser beam is diffracted by the stress-induced birefringence inside the crystal. The diffraction angle is determined from the distance between two spots exposed on a photographic plate by the first order diffracted beams as measured by a microdensitometer. The sound wavelength inside the crystal is then inferred from the laser diffraction angle. Combining the sound wavelength with the measured transducer frequency, the velocity inside the crystal is determined typically to a precision of 0·05 per cent. In this method, the measurement of velocity is not dependent on either the determination of sample length or on phase shifts at sample-transducer interface. Velocities of four pure modes, $L/\!/[001]$, $T/\!/[001]$, $L/\!/[110]$, and $T/\!/[110](P/\!/[1\bar{1}0]$ are measured in the temperature range between 293 and 423 °K. A linear temperature dependence is fit to the data by a least square method. Values obtained at 25 °C from this linear fit are

$$V_p[001] = 8{\cdot}869 \pm 0{\cdot}013 \text{ km s}^{-1},$$
$$(\partial V/\partial T)_p = -(3{\cdot}14 \pm 0{\cdot}13) \times 10^{-4} \text{ km s}^{-1} \text{ °K}^{-1};$$
$$V_s[001] = 6{\cdot}5666 \pm 0{\cdot}0055 \text{ km s}^{-1},$$
$$(\partial V/\partial T)_p = -(1{\cdot}47 \pm 0{\cdot}10) \times 10^{-4} \text{ km s}^{-1} \text{ °K}^{-1};$$
$$V_p[110] = 10{\cdot}199 \pm 0{\cdot}011 \text{ km s}^{-1},$$
$$(\partial V/\partial T)_p = -(3{\cdot}20 \pm 0{\cdot}15) \times 10^{-4} \text{ km s}^{-1} \text{ °K}^{-1};$$
$$V_s[110](P/\!/[1\bar{1}0]) = 4{\cdot}2101 \pm 0{\cdot}0043 \text{ km s}^{-1},$$
$$(\partial V/\partial T)_p = -(2{\cdot}07 \pm 0{\cdot}06) \times 10^{-4} \text{ km s}^{-1} \text{ °K}^{-1}.$$

The temperature dependence of the adiabatic elastic constants and bulk and shear (VRH average) moduli is computed using the density and

literature value of thermal expansion coefficient. Values obtained are:

$$C_{11}^s = 2814 \pm 8\,\text{kb},\ (\partial C_{11}^s/\partial T)_p = -0{\cdot}258 \pm 0{\cdot}018\,\text{kb}\,^\circ\text{K}^{-1};$$

$$C_{12}^s = 1546 \pm 9\,\text{kb},\ (\partial C_{12}^s/\partial T)_p = -0{\cdot}107 \pm 0{\cdot}019\,\text{kb}\,^\circ\text{K}^{-1};$$

$$C_{44}^s = 1543 \pm 3\,\text{kb},\ (\partial C_{44}^s/\partial T)_p = -0{\cdot}101 \pm 0{\cdot}010\,\text{kb}\,^\circ\text{K}^{-1};$$

$$K_s = 1969 \pm 6\,\text{kb},\ (\partial K_s/\partial T)_p = -0{\cdot}157 \pm 0{\cdot}014\,\text{kb}\,^\circ\text{K}^{-1};$$

$$\mu_{VRH} = 1080 \pm 5\,\text{kb},\ (\partial \mu_{VRH}/\partial T)_p = -0{\cdot}094 \pm 0{\cdot}008\,\text{kb}\,^\circ\text{K}^{-1}.$$

A comparison with previous measurements by pulse superposition and ultrasonic interferometry methods is made. Disagreement, when present, is discussed in terms of the separate measuring techniques. Finally, the present method, with its possibility for further improvement, is evaluated as a new method to measure temperature and pressure dependence of elastic constants.

1. Introduction

The most accurately determined local parameters in the interior of the Earth are density, compressional velocity, and shear velocity. These are found by inversion of body wave, surface wave, and free oscillation data, e.g. Jordan & Anderson (1974). From the density profile, the pressure at different depths can be calculated using straightforward integration. Temperature estimates for the Earth's interior depend upon assumptions regarding the distribution of heat sources, conductivity, and initial and boundary conditions, and are not well determined.

The purpose of laboratory experimental geophysics is to reproduce the pressure and temperature conditions inside the Earth in order to measure the physical properties of various minerals. Together with petrological studies, constraints can then be put on the composition and crystal structures of the material at various depths inside the Earth.

Since sound wave velocities in the Earth are so well determined from seismology, measurement of sound velocities is an important programme in experimental geophysics.

Unfortunately, direct measurement of velocities as a function of temperature and pressure is possible only over a limited range of these parameters. To date, the practical limit of measurement under pressure is 30 kb (Christensen 1974) and that of measurement under simultaneous pressure and temperature is 10 kb and 800 °K (Spetzler 1970); the latter condition corresponds roughly to a depth of 30 km.

In order to use measurements of such limited experimental range, averaging schemes to determine sound velocities of aggregates from measured component minerals, extrapolation using lattice dynamics (Sammis 1972), and finite strain theories (Anderson, Sammis & Jordan 1972) must be employed to infer the physical and chemical states at greater depths. To date, the methods with the highest precision for measuring pressure and temperature dependence of sound velocities in solids are the ultrasonic methods by pulse superposition (McSkimin 1961; McSkimin & Andreatch 1962), by the gated double-pulse interferometry with a buffer rod (Spetzler 1970), and by the pulse-echo-overlap technique (Papadakis 1967). Natural rocks, because of porosity and grain boundary scattering of ultrasonic pulse trains, cannot be subjected to this method of measurement. Some artificially sintered polycrystalline samples, notably Al_2O_3 and MgO polycrystalline aggregates, although measurable by this method, show hysteresis when cycled in pressure and temperature (Spetzler & Anderson 1971). It seems that single crystals are the only samples that can be measured reliably by the methods of ultrasonic interferometry, and data on various geophysically important minerals measured by the first two of the three ultrasonic

methods already exist (Anderson *et al.* 1968; Graham & Barsch 1969; Spetzler 1970; O'Connell & Graham 1971; Frisillo & Barsch 1972; Chang & Barsch 1973).

Although the methods of ultrasonic interferometry has very high precision, systematic errors arising from the boundary condition at the crystal-transducer or crystal-buffer rod interface are difficult to ascertain and measurements on pressure and temperature dependence of sound velocities from different laboratories on the same mineral differ sometimes by as much as 25 per cent. Clearly, this is a basic limitation on extrapolation of laboratory measurements to mantle conditions.

The present work is an attempt to use an independent method, the method of light-sound scattering in the Raman–Nath region, to measure the temperature dependence of single-crystal sound velocities.

The interaction of light and sound in the Raman–Nath region was first observed in liquid by Debye & Sears (1932) and in solid by Schaefer & Bergmann (1934). This method was employed at that time to determine the elastic constants of various crystals and the results are summarized in Bergmann (1954). Their experimental accuracy was limited by the technology at that time which lacked a coherent laser light source, a fast and high resolution photographic plate, and a photographic density read-out instrument with high positional accuracy. As a consequence, neither temperature nor pressure dependence of single-crystal elastic constants has ever been measured by this technique until the present work.

Temperature dependence of sound velocities in single-crystal spinel $MgAl_2O_4$, chosen because of the availability of high quality synthetic spinel crystals, the existence of previous measurements by ultrasonic interferometry methods, and its geophysical importance, was successfully measured in the present experiment. The temperature dependence of the elastic constants was determined from these data.

2. Interaction between light and sound—a theoretical background

The index of refraction ellipsoid in its general form is

$$B_{11}x^2+B_{22}y^2+B_{33}z^2+2B_{23}yz+2B_{31}zx+2B_{12}xy = 1 \tag{1}$$

Let $B_{11} \equiv (1/n^2)_{xx}$, $B_{22} \equiv (1/n^2)_{yy}$, $B_{33} \equiv (1/n^2)_{zz}$, $B_{23} \equiv (1/n^2)_{yz}$, etc., and use the notation $x \to x_1$, $y \to x_2$, $z \to x_3$, $11 \to 1$, $22 \to 2$, $33 \to 3$, $23 \to 4$, $31 \to 5$, $12 \to 6$. Assume also that the indicatrix is diagonalized in the absence of external stress. In the presence of external stress, the change in B_{jl} is

$$\delta B_{jl} = \pi_{jlmn}\sigma_{mn} = p_{jlmn}\varepsilon_{mn} \tag{2}$$

where

σ_{mn} = stress tensor, ε_{mn} = strain tensor

π_{jlmn} = piezo-optical coefficients

p_{jlmn} = elasto-optical coefficients.

Spinel, a cubic crystal belonging to space group O_h^7(Fd3m) has piezo-optical coefficients of the form (Nye 1957):

$$(\pi_{jlmn}) = \begin{pmatrix} \pi_{11} & \pi_{12} & \pi_{12} & & & \\ \pi_{12} & \pi_{11} & \pi_{12} & & & \\ \pi_{12} & \pi_{12} & \pi_{11} & & & \\ & & & \pi_{44} & & \\ & & & & \pi_{44} & \\ & & & & & \pi_{44} \end{pmatrix}. \tag{3}$$

For example, a uniaxial compressional stress of magnitude σ applied in the x_1-direction would give the change in (B_{jl}) as

$$\begin{pmatrix} \delta B_1 \\ \delta B_2 \\ \delta B_3 \\ \delta B_4 \\ \delta B_5 \\ \delta B_6 \end{pmatrix} = \begin{pmatrix} \pi_{11} & \pi_{12} & \pi_{12} & & & \\ \pi_{12} & \pi_{11} & \pi_{12} & & & \\ \pi_{12} & \pi_{12} & \pi_{11} & & & \\ & & & \pi_{44} & & \\ & & & & \pi_{44} & \\ & & & & & \pi_{44} \end{pmatrix} \begin{pmatrix} \sigma \\ 0 \\ 0 \\ 0 \\ 0 \\ 0 \end{pmatrix} \tag{4}$$

which implies

$$\begin{aligned} \delta n_1 &= -\tfrac{1}{2}(n^0)^3\,\delta B_1 = -\tfrac{1}{2}(n^0)^3\,\pi_{11}\,\sigma \\ \delta n_2 &= \delta n_3 = -\tfrac{1}{2}(n^0)^3\,\pi_{12}\,\sigma \\ \delta n_4 &= \delta n_5 = \delta n_6 = 0, \end{aligned} \tag{5}$$

i.e. the crystal becomes birefringent, but the indicatrix has the same principal axes. In the more general case, the principal axes would have been rotated as well. When the external stress has a sinusoidal dependence (a stress wave), an indicatrix variation wave also passes through the crystal. This periodic change in the index of refraction inside the crystal diffracts light as a grating and is the basis of scattering of light by sound.

The index of refraction tensor is related to the dielectric tensor (ε_{jl}) by

$$\frac{1}{n_{jl}^2} = \frac{1}{\varepsilon_{jl}}, \quad (\varepsilon_{ij}) \equiv (B_{ij})^{-1}. \tag{6}$$

The electric displacement vector is given by (in esu units)

$$\mathbf{D} = \mathbf{E} + 4\pi\mathbf{P} \tag{7}$$

where

$\mathbf{E}$ = electric field vector,

$\mathbf{P}$ = polarization vector.

In the component form

$$P_j = \frac{1}{4\pi}(\varepsilon_{jl} - \delta_{jl})E_l \tag{7a}$$

where δ_{jl} is the Kronecker delta.
The change in polarization due to external stress can be derived as follows:
From (7a)

$$\delta P_j = \frac{1}{4\pi}(\delta\varepsilon_{jl})E_l \tag{8}$$

when $j = l$, for example, $j = l = 1$

$$\delta\left(\frac{1}{n^2}\right)_{11} = \delta\left(\frac{1}{\varepsilon_{11}}\right) = -\frac{\delta\varepsilon_{11}}{\varepsilon_{11}\,\varepsilon_{11}} \tag{9}$$

when $j \neq l$, for example, $j = 1$, $l = 2$. Since $(\varepsilon_{ij}) \equiv (B_{ij})^{-1}$

$$B_{12} = -\begin{vmatrix} \varepsilon_{12} & \varepsilon_{13} \\ \varepsilon_{32} & \varepsilon_{33} \end{vmatrix} \Big/ \det|\varepsilon_{ij}|. \tag{10}$$

Assume $\varepsilon_{jl} \ll \varepsilon_{11}, \varepsilon_{22}, \varepsilon_{33}$, i.e. the effect of external stress is small on the indicatrix.

$$\delta B_{12} = B_{12} = -\varepsilon_{12}/\varepsilon_{11}\,\varepsilon_{22} = -\delta\varepsilon_{12}/\varepsilon_{11}\,\varepsilon_{22}. \tag{11}$$

Combining (2), (9), and (11)

$$\delta B_{jl} = -\delta\varepsilon_{jl}/\varepsilon_{jj}\,\varepsilon_{ll} = \pi_{jlmn}\,\sigma_{mn} \tag{12}$$

$$\delta\varepsilon_{jl} = -\varepsilon_{jj}\,\varepsilon_{ll}\,\pi_{jlmn}\,\sigma_{mn}. \tag{12a}$$

Substitute (12a) into (8), with superscript i to indicate incident light,

$$\delta P_j = -\frac{1}{4\pi}\,\varepsilon_{jj}\,\varepsilon_{ll}\,\pi_{jlmn}\,\sigma_{mn}\,E_l^{(i)} \tag{13}$$

which is the non-linear source term in Maxwell's equations that couples sound wave σ_{mn} and incident light $E_l^{(i)}$ to generate the diffracted light.

The diffracted light can be represented in terms of scalar and vector potentials Φ, A, respectively, as

$$\mathbf{E}^{(d)} = -\nabla\Phi - \frac{1}{c}\frac{\partial \mathbf{A}}{\partial t} \tag{14}$$

with

$$\left.\begin{aligned} \Phi &= -\int d^3x' \int dt' \frac{\nabla'.\delta\mathbf{P}(\mathbf{x}', t)}{|\mathbf{x}-\mathbf{x}'|}\,\delta\left(t'-t+\frac{|\mathbf{x}-\mathbf{x}'|}{c}\right) \\ \mathbf{A} &= \frac{1}{c}\int d^3x' \int dt' \frac{\partial\delta\mathbf{P}(\mathbf{x}', t)}{\partial t'}\left(t'-t+\frac{|\mathbf{x}-\mathbf{x}'|}{c}\right)\Big/|\mathbf{x}-\mathbf{x}'| \end{aligned}\right\} \tag{15}$$

where c is the velocity of light.

Let both incident light and acoustic waves be monochromatic plane waves (since the diffracted light field is linear in the amplitudes of incident light and acoustic fields, more general fields can be represented by superposition):

$$\left.\begin{aligned} \mathbf{E}^{(i)}(\mathbf{x}, t) &= \mathbf{E}^{(i)0}\exp\left[i(\mathbf{k}^{(i)}.\mathbf{x}-\omega^{(i)}t)\right] \\ \sigma_{mn}(x, t) &= \textstyle\sum_{mn}\exp\left[i(\mathbf{K}.\mathbf{x}-\Omega t)\right] \\ \mathbf{E}^{(d)}(x, t) &= \mathbf{E}^{(d)0}\exp\left[i(\mathbf{k}^{(d)}.\mathbf{x}-\omega^{(d)}t\right]. \end{aligned}\right\} \tag{16}$$

On substituting (16) into (13), then into (15), and finally into (14), Hope (1968), for example, showed that

$$\left.\begin{aligned} \omega^{(d)} &= \omega^{(i)}+l\Omega \\ \mathbf{k}^{(d)} &= \mathbf{k}^{(i)}+l\mathbf{K}, \quad l = \text{integer or zero.} \end{aligned}\right\} \tag{17}$$

These are conservation laws of energy and pseudomomentum. The same conservation laws can also be derived by quantum mechanical means if one quantizes the acoustic and electromagnetic fields, expresses the interaction between acoustic and electromagnetic fields as a perturbation Hamiltonian, and solves the equation of motion for the boson operators. However, the classical treatment is sufficient for the present purpose. The conservation laws hold regardless of crystal symmetry.

In an isotropic crystal or in anisotropic crystals when the diffracted light has the same index of refraction as the incident light, the light-sound scattering takes the relatively simple form of normal Bragg diffraction, and in the long acoustic wavelength limit, Raman–Nath scattering.

The more complicated case of light-sound scattering in an anisotropic crystal when the diffracted light experiences a different index of refraction from the incident light is discussed by Dixon (1967) and by Hope (1968). The results are omitted here because the experimental technique of the present study is derived from Raman–Nath scattering.

The difference between normal Bragg scattering and Raman–Nath scattering has been discussed by Extermann & Wannier (1936), by Willard (1949), and by Klein & Cook (1967). The results can be summarized as follows:

The important parameters are

$$v = 2\pi(\delta n)t/\lambda_0, \quad Q = 2\pi\frac{\lambda_0}{\Lambda^2}t/n_0, \quad \alpha = -\frac{n_0\Lambda}{\lambda_0}\sin\theta$$

where

δn = amplitude of index of refraction variation experienced by the polarization vector,

λ_0 = light wavelength in vacuum,

t = width of the acoustic wave column,

Λ = acoustic wavelength,

θ = angle between light wave vector and sound wavefront,

n_0 = index of refraction experienced by the polarization vector in the absence of sound waves.

Refer to Fig. 1. From energy and momentum conservation relations (13),

$$\left.\begin{aligned}\sin\phi_l &= (k\sin\theta + lK)c/(\omega + l\Omega)\\ &= \sin\theta + l\frac{\lambda}{\Lambda}\end{aligned}\right\} \tag{18}$$

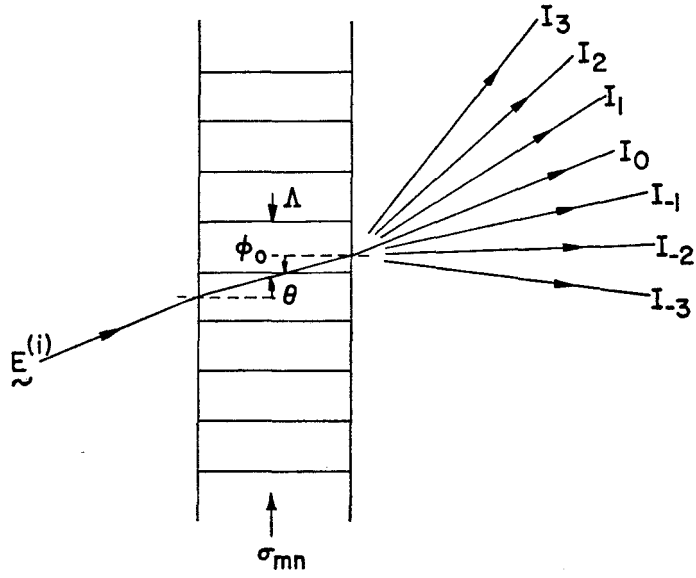

FIG. 1. Schematic representation of light-sound scattering in the Raman–Nath region.

since

$$\Omega/\omega = 3\times10^{7}\Big/\frac{3\times10^{10}}{0{\cdot}63\times10^{-4}} = 0{\cdot}63\times10^{-7} \ll 1$$

for 30 MHz acoustic wave scattering light at 0·63-μm wavelength. The sound wave acts like a phase grating in the limit of narrow width and low frequency. This is known as the Raman–Nath diffraction. The diffracted light intensities can be described by the analytic expression

$$I_l = J_l{}^2\left[v\frac{\sin(Q\alpha/2)}{(Q\alpha/2)}\right], \quad J_l = \text{Bessel function of order } l, \tag{19}$$

which implies that many diffraction orders are observed, the diffraction intensity pattern is symmetric with respect to the zeroth order at all angles of incidence and that oblique incidence has the effect of reducing the value v by the factor $\sin(Q\alpha/2)/(Q\alpha/2)$. The region for which the expression (19) is a good approximation is defined by

$$Qv \leqslant \frac{\pi^2}{4} \quad \text{and} \quad Q \ll 2. \tag{20}$$

As the value of Q increases beyond (20), the simple expression given by (19) does not hold for the diffracted intensities. Firstly, more light appears in the lower diffraction orders than predicted by (19) and secondly, with respect to angle of incidence, the zeroth order is symmetric about normal incidence whereas the first orders are symmetric about their respective Bragg angles $\alpha_B = \pm\frac{1}{2}$. As Q approaches the limit $Q \gg 1$, only positive and negative first orders appear besides the zeroth order for the incident angle $\alpha = \frac{1}{2}$ and $\alpha = -\frac{1}{2}$, respectively. The intensity is given by

$$\left.\begin{aligned} &I_0 = \cos^2(v/2), \quad I_1 = \sin^2(v/2) \\ \text{or} \quad &I_0 = \cos^2(v/2), \quad I_{-1} = \sin^2(V/2). \end{aligned}\right\} \tag{21}$$

For example, take $\alpha = -\frac{1}{2}$, $\sin\theta = \lambda/2\Lambda$, and (18) implies

$$\sin\phi_{-1} = -\frac{\lambda}{\Lambda} + \sin\theta = -\frac{\lambda}{2\Lambda} = -\sin\theta = \sin(-\theta) \tag{22}$$

which is the familiar Bragg condition.

Physically, the distinction between the Raman–Nath limit and the Bragg limit is that, in the Bragg limit, the width of the sound wavefront is not negligible as is the case with Raman–Nath diffraction and no resulting diffracted light can be observed unless light scattered from different parts of the same wavefront add up in phase.

3. Experimental method

3.1 *Experimental setup and procedure*

The experimental setup is illustrated schematically in Fig. 2. The light source is derived from a Spectra Physics Model 135, 3 mW He–Ne laser which oscillates at 0·6328 μm, has a random polarization and operates in the TEM_{00} mode. The laser beam is spatial filtered by a microscope objective which focuses the beam through a 25-μm pinhole. After spatial filtering, the laser beam is focused on the photographic plate by a second microscope objective. The reflecting mirror in the setup is flat to a tenth of a wavelength of sodium light. The sample in the sample holder is spring loaded in a tubular furnace with one spacer block at each end. The cross-section of

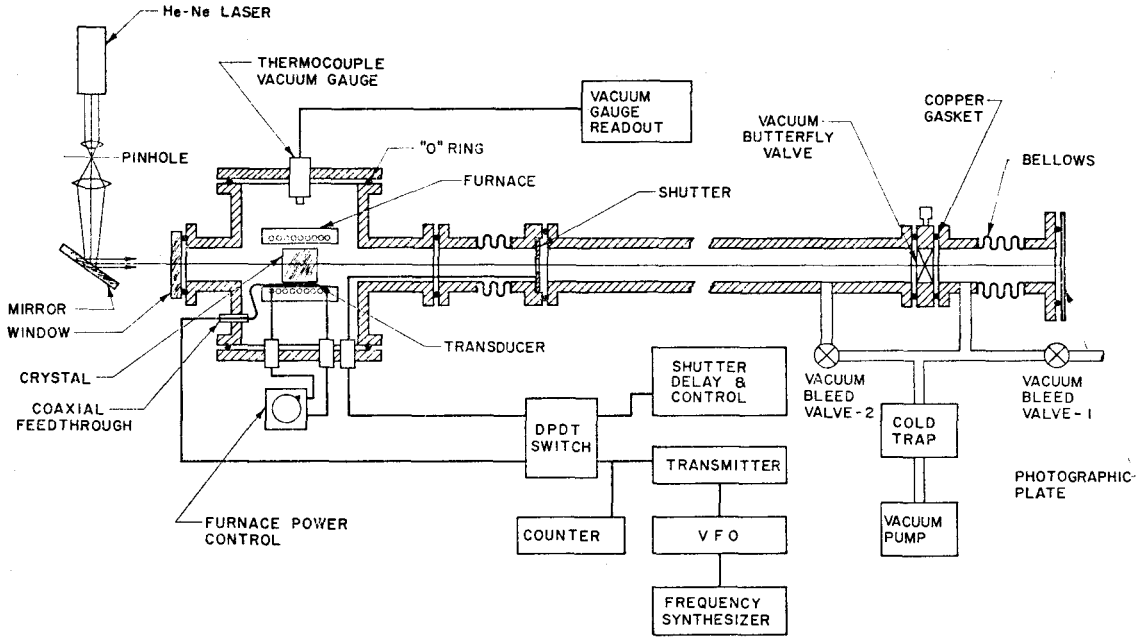

FIG. 2. Schematic diagram showing experimental setup for light-sound scattering measurement of temperature dependence of single crystal elastic constants.

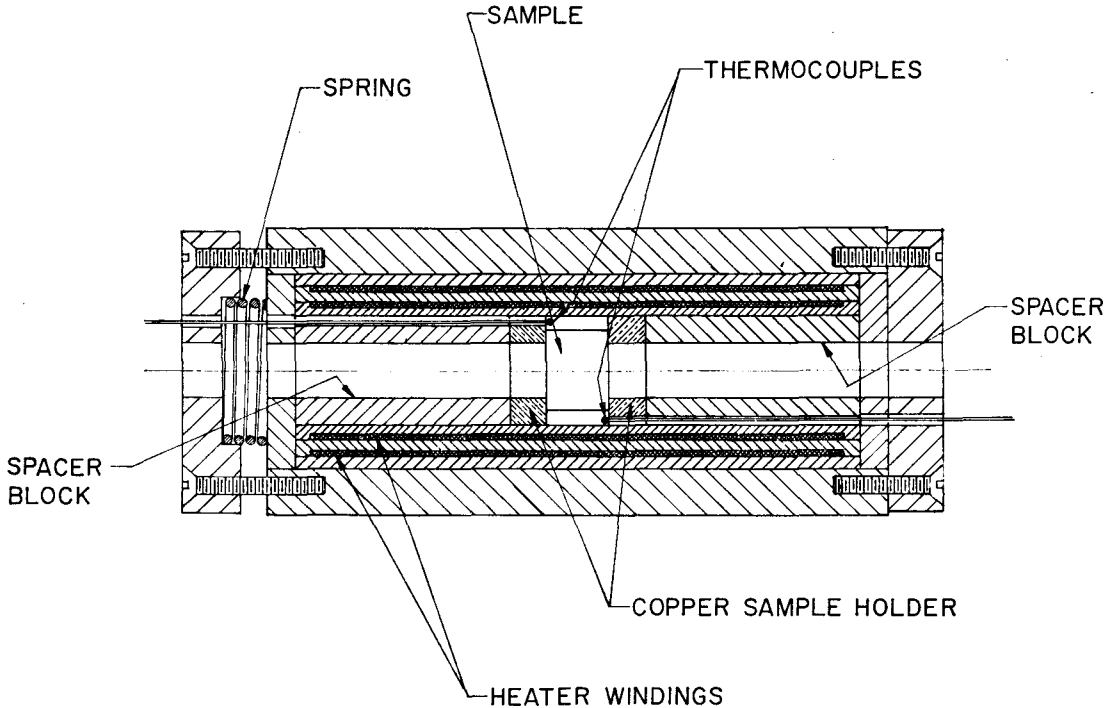

FIG. 3. Furnace cross-section through thermocouple with sample in place.

the furnace assembly through the two thermocouples is shown in Fig. 3. The furnace is latched with springs on two V-blocks which are bolted to a translation stage with translation direction perpendicular to the laser beam. The translation stage is bolted to the base plate of a vacuum tank. The translation stage and the levelling screws on the base plate are used to position the crystal such that the laser beam would go through inside the crystal once it is aligned perpendicular to the crystal face. The dimension of the vacuum tank is about 203 cm inside diameter and 30·5 cm high. The distance between the sample and photographic plate is about 258 cm. The vacuum system is sealed by an optical flat at the entrance end of the laser beam and is sealed by a photographic plate at the opposite end. The photographic plate holder is coupled to an anchoring block by screws, and nuts are used, when pushed against the vacuum pull, to orient the photographic plate plane parallel to the sample. The optical components, the vacuum tank, and the photographic plate holder anchoring block are rigidly glued to a granite table by epoxy for stability. The purpose of the evacuated tank is to have the light path between sample and the recording photographic plate under partial vacuum so as to reduce index of refraction fluctuation which would otherwise introduce random error into the data. The working vacuum during the experiment is between 85 and 180 μm of mercury as measured by a thermocouple vacuum gauge. The vacuum butterfly valve is employed to avoid letting air into the whole system during photographic plate change. The ultrasonic forced vibration inside the sample is generated by a lithium niobate transducer (30 MHz centre frequency) coupled to the sample with Nonaq stopcock grease and spring loaded through a gauge block onto the sample. The RF signal is generated by a Heathkit variable frequency oscillator whose output frequency is synchronized to a Schomandl frequency synthesizer. The output of the variable frequency oscillator is used to drive a Heathkit transmitter which also quadruples the frequency at the same time. The output of the transmitter is fed into the vacuum system to the transducer electrodes through a section of Uniform Tubes UT-250SS vacuum tight coaxial cable. The frequency of the RF signal is measured by a Systron-Donner frequency counter. The Uniblitz shutter in the setup is controlled by two relays and the shutter power supply and drive unit. The relays control the time interval during which a 5 volt signal is applied to the switching circuit which keeps the shutter open. A DPDT switch is used to switch both the transmitter and the shutter relays. The first relay is delayed 50 ms relative to the closing of the switch. Since the transmitter has a rise time of 0·3 ms, a steady state vibration is well setup inside the crystal at the opening of shutter by the first relay. The furnace power is controlled by a Variac power supply whose primary voltage is regulated to stay stable at 115 volts. Temperatures inside the furnace are measured by two alumel–chromel thermocouples. These two thermocouples are located at about 0·1 cm from the sample. During a separate calibration run, a third thermocouple is pasted with Sauereisen cement directly on the sample surface where the laser beam would leave the crystal, to measure the temperature difference at the sample and at the thermocouple sites. The calibration results will be discussed in Section 3.3. The thermocouple voltage output is read with a Hewlett–Packard multifunction meter.

During the experiment, the laser beam is aligned perpendicular to the crystal face by the angular orientation device holding the mirror. The photographic plate plane is then aligned parallel to the crystal face by sealing the end bellows section of the vacuum system with an optical flat and using an auxiliary mirror behind the optical flat. The beam reflected from the auxiliary mirror is made to coincide with the incident beam. Part of the reflected beam is reflected again at the optical flat sealing the end bellows section. This reflected beam is used to guide the adjustment of the plate holder orientation screws. The parallelism between photographic plate and crystal surface and the perpendicularity between laser beam and crystal surface can be adjusted to within 1 mrad with relative ease.

The synthesizer frequency is adjusted approximately for the creative interference condition of the forced vibration in the direction perpendicular to the transducer. This can be judged by the intensity of the diffracted light. After evacuation of the optical path between crystal and photographic plate, the DPDT switch is thrown and the photographic plate is exposed to the diffracted beams. The undiffracted central beam is blocked off before it reaches the photographic plate. The photographic plates used in the experiments are Agfa-Gavaert 8E-75 high resolution (3000 lines/mm) and 10E-75 high resolution (2800 lines/mm) photographic plate with antihalation back coating. The size of the plates is 10·2 by 12·7 mm. Immediately after exposure, the plate is processed in Kodak D-19 developer for 6 min, in glacial acetic acid stop bath for 30 s, in Kodak Rapid Fix for 5 min and followed by washing and drying.

The distance between photographic plate and sample is measured with Starrett inside micrometers (Table 6).

3.2 *Sample description*

The sample is a single-crystal stoichiometric $MgAl_2O_4$ spinel grown by the Czochralski method and furnished by the Crystal Products Division of Union Carbide Corporation. After being rough cut, the boule is lapped into a prism with two sets of faces parallel to (001) and (110) respectively. The crystal orientation is determined to be $5\pm5'$ parallel to (001) and $0\pm5'$ parallel to (110) by the Laue back reflection method. The final polish of the two sets of faces to a tenth wavelength of sodium light flat and laser finish is done by Crystal Optics of Ann Arbor, Michigan. The parallelism between the polished faces is less than 10 sec of arc. The dimension of the sample is $0{\cdot}8923\pm0{\cdot}0002$ cm (between (001) faces) $\times$ $1{\cdot}1793\pm0{\cdot}0002$ cm (between (110) faces) $\times$ $1{\cdot}2578\pm0{\cdot}0002$ cm (between the unpolished (110) faces). The density of the sample is measured by liquid immersion method to be $3{\cdot}5784\ g\,cm^{-3}$ at 25 °C. The sample is also placed between two crossed polarizers and illuminated by a diffused light source to examine for residual stress. No residual stress is found within the sample between the two sets of faces both before and after the experiment.

3.3 *Data and data reduction*

The data as recorded (raw data) are two dark spots exposed by the diffracted laser beams on a photographic plate. A contact print made from such a photographic plate is shown in Fig. 4. The distance between the two spots is measured on the optical density read-out recorder chart from a Joyce–Loebl double beam microdensitometer. The procedure is described below. The photographic plate is placed on the microdensitometer stage with its bottom edge pushed against the bottom edge of the recessed stage. The direction defined by the two spots on the photographic plate is aligned parallel to the scanning direction of the microdensitometer by rotating the stage and observing the images of the two spots with respect to a pair of cross-hair on the microdensitometer viewing screen. Alignment error is $\pm0{\cdot}1°$. The angle between the direction defined by the spots and bottom edge of the photographic plate, γ, is read off the stage rotation table. A Starrett no. 362 precision protractor is then placed on top of the photographic plate with its square frame set against the edge of the microdensitometer stage. The protractor angle is set at the angle γ but in an opposite sense. The vernier on the Starrett protractor reads to one-twelfth of a degree. An American Optical Corporation AO1400 stage micrometer is laid on top of the two spots and against the blade of the precision protractor. The positioning of the protractor angle puts the scale divisions on the stage micrometer perpendicular to the microdensitometer travel direction. The purpose of the stage micrometer is to put fiducial marks on the microdensitometer read-out chart for distance measurement. The photographic plate, Starrett protractor, and the stage micrometer are fixed in position on the microdensitometer stage by spring clips. An example of the micro-

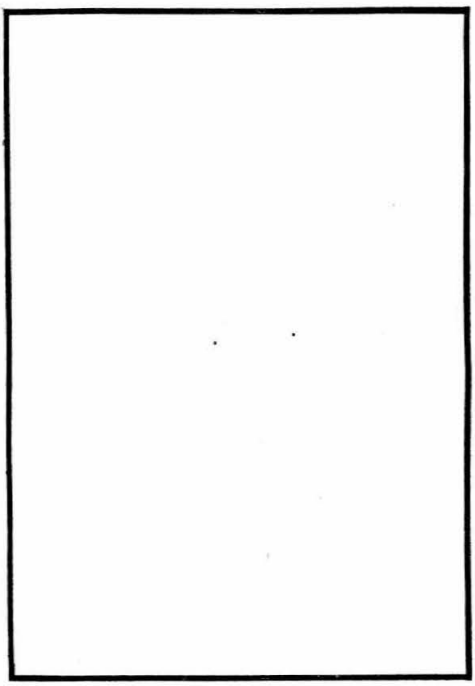

FIG. 4. Contact print made from a data photographic plate.

densitometer read-out with this arrangement are shown in Fig. 5. Since it is the change of distance that is important in the temperature dependence measurement, the two spikes marked '4 mm' and '14 mm' are used as fixed fiducial marks in an entire suite of measurements. (For example, $V_p[100]$ from 293 to 423 °K.) The two density profiles are then matched on a light table and a pencil mark is put on both charts at the same (but arbitrary) location. The distance between the spots is therefore equal to a fixed distance (distance between the fiducial marks '4 mm' and '14 mm) plus the distance from the pencil mark on Fig. 5(a) to '4 mm' and the distance from the pencil mark on Fig. 5(b) to '14 mm'. The scale on the charts is provided by the distance between the fiducial marks '3 mm' and '4 mm', and '14 mm' and '15 mm', respectively. Those distances are calibrated by American Optical Corporation to be $0{\cdot}1 \pm 0{\cdot}0005$ cm. The use of fiducial marks is necessitated by the limited travel of the microdensitometer stage at large magnification (approximately 200 to 1). The distance between the two spots in Fig. 5(a) and (b) is then read as

$$l = 10\,\text{mm} + \left(\frac{9{\cdot}23 \pm 0{\cdot}01}{19{\cdot}75 \pm 0{\cdot}01} + \frac{\binom{6{\cdot}98}{6{\cdot}71} \pm 0{\cdot}01}{19{\cdot}81 \pm 0{\cdot}01} \right) \text{mm} \qquad (23)$$

where 10 mm is the distance between the fixed fiducial marks '4 mm' and '14 mm'. 9·23 is the distance in centimetres on the chart from the pencil mark on Fig. 5(b) to the '14 mm' marker. 19·75 is the distance in centimetres on the chart between the fiducial marks '14 mm' and '15 mm' on the same figure. The corresponding readings on Fig. 5(a) are $\binom{6{\cdot}98}{6{\cdot}71}$, and 19·81. There are two readings, 6·98 and 6·71 because the two density profiles are not identical, and there is a latitude in which 'matching

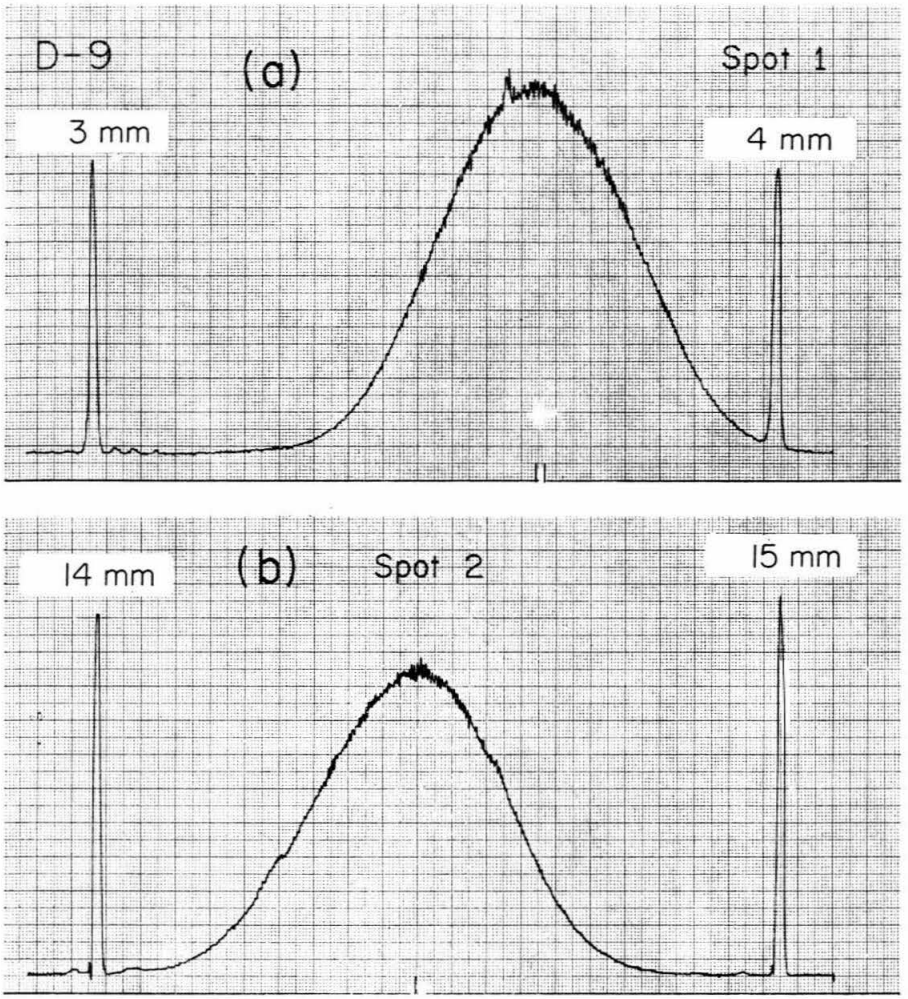

FIG. 5. (a) Microdensitometer trace out of photographic plate D-9, spot 1. (b) Microdensitometer trace out of photographic plate D-9, spot 2.

of the two density profiles can be considered as equally good. In the present case 6·98 is the distance in centimetres on the chart from the pencil mark to the '4 mm' marker when matching is by the top part of the density profiles. 6·71 is the corresponding distance when matching is by the bottom part of the density profiles. These are illustrated in Figs 6 and 7. This latitude in matching is indeed the major source of experimental uncertainty, and will be discussed in detail later. A measure of the reproducibility of the microdensitometer read-out is provided by the repeated optical density read-outs of divisions on the stage micrometer used as fiducial markers. Histograms of the distribution of repeated read-out of distance between pairs of markers are shown in Fig. 8. It is estimated from these histograms that the repeatability of intensity profiles is within 0·05 cm on the microdensitometer recorder chart. Note that in Fig. 8 the distance between the two markers '5 mm' and '6 mm' in the data read-out for V_s[001] differs from that in the data read-out for V_p[110]. This is because the ratio arm connecting the microdensitometer specimen table and recorder chart table is removed between the two read-outs, and slight variation in the setting of the ratio arm in its socket causes the difference in the two read-outs. Since the error in

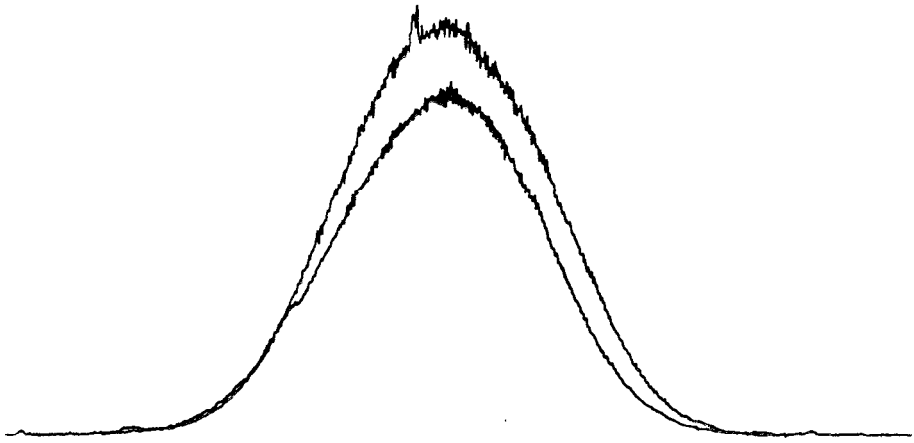

FIG. 6. Matching of the two density profiles of photographic plate D-9 by top.

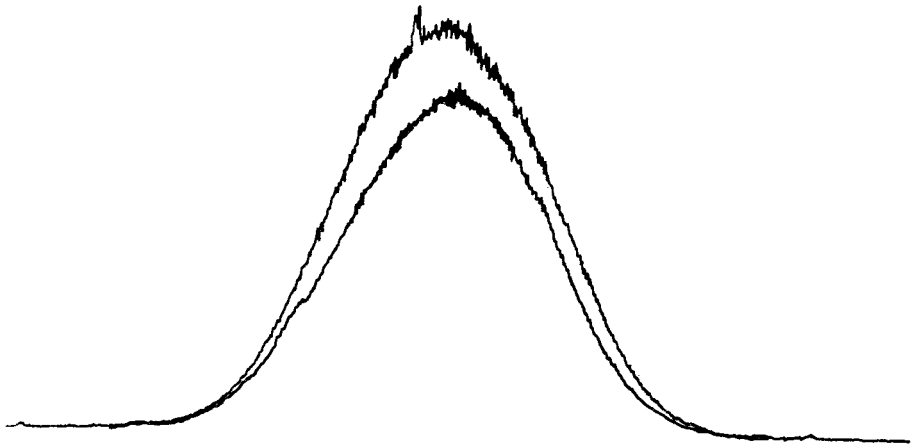

FIG. 7. Matching of the two density profiles of photographic plate D-9 by bottom.

aligning the two spots with the microdensitometer stage travel direction is $\pm 0{\cdot}1°$, and the error in aligning the stage micrometer with the two spots is also $\pm 0{\cdot}1°$, the error in distance measurement between the two spots due to angular misalignment is $l(1-\cos 0{\cdot}14°) \cong 5\times 10^{-6}\, l \cong 0{\cdot}05\ \mu$m, assuming the distance, l, to be 1 cm. This uncertainty is equivalent to 0·001 cm on the read-out chart, and is negligible compared to the latitude in density profile matching as discussed earlier.

Consider now the problem of the difference in the two density profiles on the same photographic plate. Note first that the degree of disparity varies from one photographic plate to another. Indeed, the two density profiles in Fig. 5(a) and (b) are one of the worst cases. An example of two density profiles which match better is illustrated by Figs 9(a), 9(b) and 10.

The reason for this disparity is that the stress-induced birefringence inside the crystal does not assume a plane wavefront parallel to the sample faces. Temperature gradient inside the sample, edge and corner effects, lack of perfect parallelism between

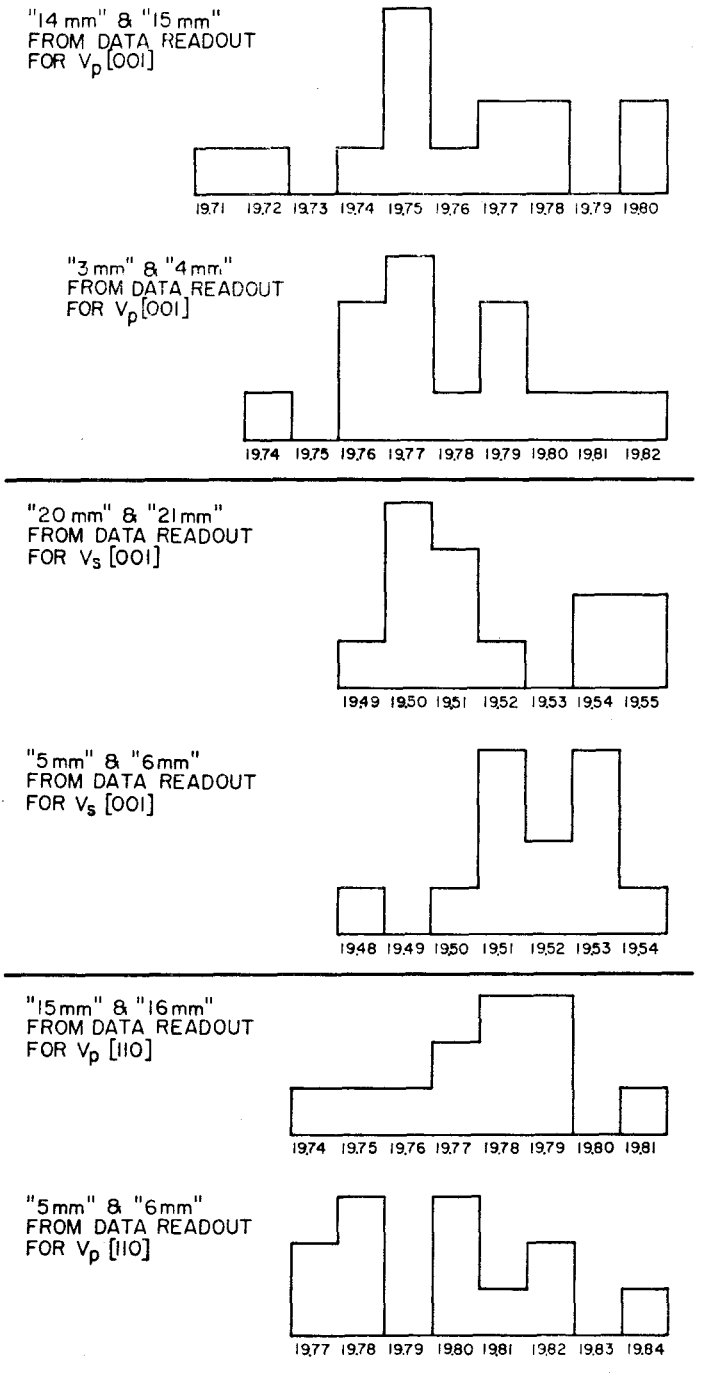

FIG. 8. Histogram giving a measure of reproducibility of density readout by a Joyce-Loebl Mk III CS microdensitometer.

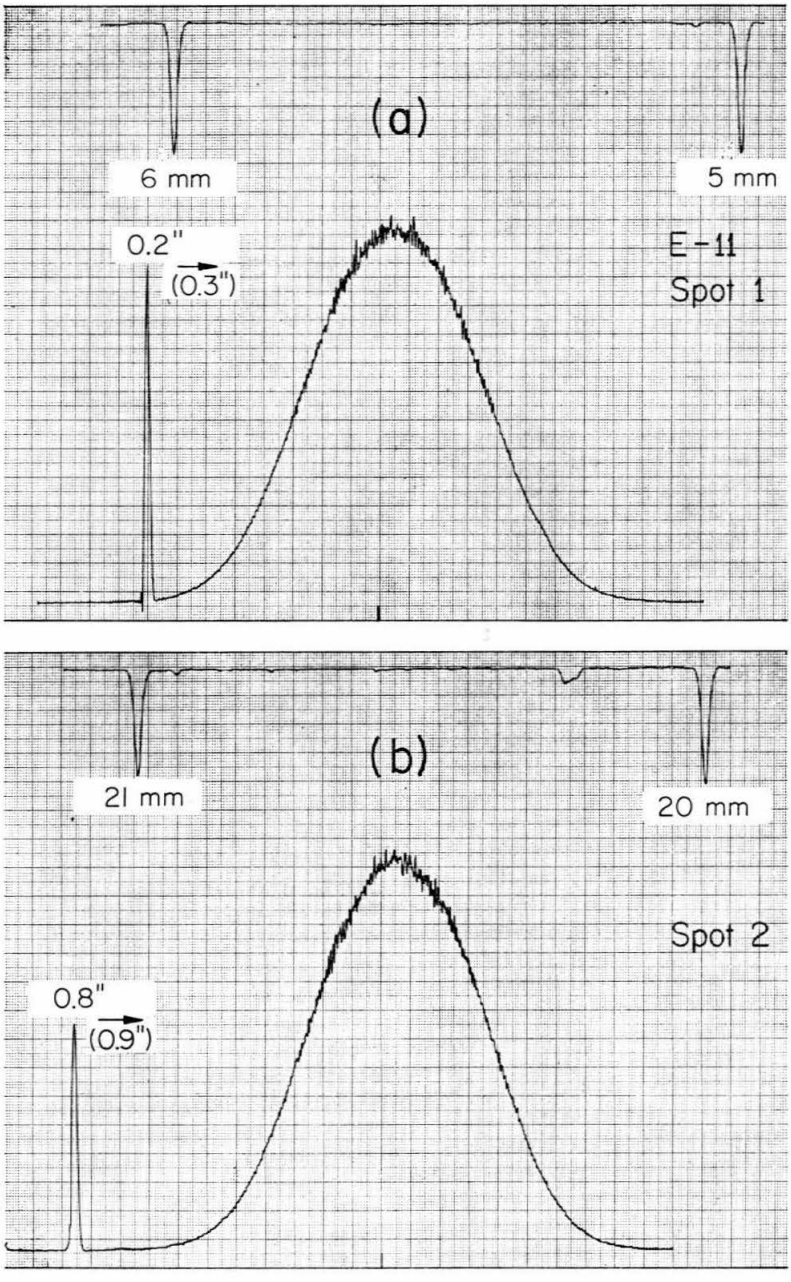

FIG. 9. (a) Microdensitometer trace out of photographic plate E-11, spot 1. (b) Microdensitometer trace out of photographic plate E-11, spot 2.

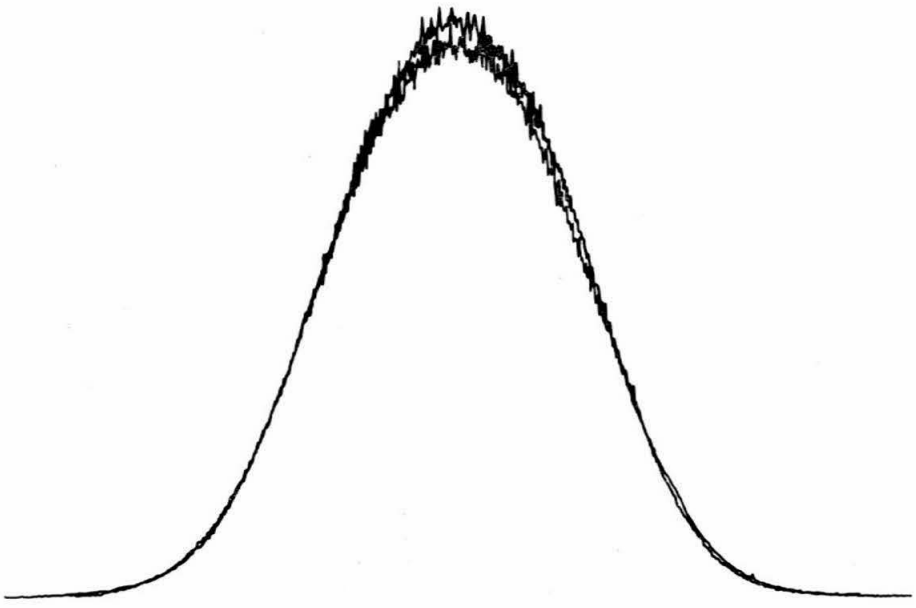

FIG. 10. Matching of the two density profiles of photographic plate E-11.

sample faces, positioning of the transducer and transducer radiation pattern all cause the steady state birefringence pattern to deviate from a plane standing wave. The laser beam in the experiment is not a collimated plane wave either, and has a convergence angle of about 1 mrad. The experiment can be analysed by first decomposing the steady-state birefringence pattern induced by forced vibration of the crystal and the laser beam into plane waves in different directions. The component plane light waves and sound waves interact according to the theory as described in Section 2 and the resultant diffracted light pattern is the superposition of the diffracted plane light waves.

Recall that as a function of incidence angle, the first order intensities are symmetric with respect to their respective Bragg angles $\alpha_B = \pm\frac{1}{2}$

$$\alpha_B = -\frac{\Lambda n_0}{\lambda_0}\sin\theta_B = \pm\tfrac{1}{2} \tag{24}$$

which implies

$$\sin\theta_B = \mp\frac{\lambda_0}{2\Lambda_0 n}. \tag{25}$$

The parameter Q is given by

$$Q = 2\pi\frac{\lambda_0 t}{\Lambda^2 n_0}. \tag{26}$$

The Bragg angle and the parameter Q for velocity measurements in different crystal directions are calculated using sound velocities at 25° C, index of refraction of spinel and the sample thickness as width of the sound column. The results are listed in Table 1. An upper limit of the parameter v can be estimated from the intensity of the first order diffracted light, which is in turn determined by the optical density of the diffracted spots on the photographic plate, by the exposure time, and by the charac-

Table 1

Bragg angle and the parameter Q for various velocity measurements

Measurement	Bragg angle (mrad)	Q
V_p[001]	0·61	0·3
V_s[001]	0·87	0·6
V_p[110]	0·56	0·3
V_s[110](P[1$\bar{1}$0])	1·36	1·1

teristic curve of the photographic plate. The upper limit of the first order diffracted light intensity for all measurements is determined to be 10 per cent of the incident laser beam. The corresponding upper limit of the parameter v is $\sim$0·65 since no second order diffracted light is recorded on the photographic plate. From (20) and numerical calculations by Klein & Cook (1967), the intensity distribution given by the Raman–Nath theory is a good approximation for the following analysis. For simplicity, the laser beam is approximated by a collimated plane wave. This involves an error of $\sim$1 mrad in direction of propagation of the various component plane waves of the laser beam. Divide the component sound plane waves into those whose wave vectors are perpendicular to the light wave vector and those which do not belong to the class just described. For plane sound waves whose wave vectors are perpendicular to the light wave vector, the diffracted first-order light intensity is given by (14) with $\alpha = 0$ and $l = 1$, i.e. $I_1 = J_1^2(v)$. (This assumes the Raman–Nath limit that the Bragg angle is 0°, which introduces an error of at most 1·36 mrad as seen from Table 1.) By adjusting the transducer driving frequency, however, only plane waves whose wave vector lies nearly perpendicular to the polished faces (on one of which the transducer is mounted) can enjoy the condition of constructive interference. The result is demonstrated in Fig. 4. Since all photographic plates are pushed with bottom edge against the film holder bottom orienting screws during exposure, the direction defined by the two spots relative to the photographic plate bottom edge serves to check the maximum deviation from pure mode of the sound wave velocity which each photographic plate measures. The microdensitometer table angle readings in Tables 2–5 are exactly these data. The maximum deviation angle is 0·6°. Now consider those waves in whose wave front the light wave vector does not lie. The first order diffracted light intensity from these waves is given by (20) with $l = 1$ and $\alpha \neq 0$, i.e. $I_1 = J_1^2[v \sin(Q\alpha/2)/(Q\alpha/2)]$. This intensity distribution as a function of α is plotted in Klein & Cook (1967) and has zeroes at $Q\alpha = 2m\pi$ where n is any non-zero integer. The intensity is significant only for values of α less than the first zero. The first zero occurs at $\alpha = 2\pi/Q$ which implies $|\sin\theta| = \Lambda/t$. Take t to be width of the sample and using sound velocities at 25 °C, $\theta \cong 1° 30'$ for V_p[100] measurements, 1° for V_s[100] measurements, 2° for V_p[110] measurements, and 0° 50′ for V_s[110] measurements. Since the characteristic curves of the Agfa-Gavaert 8E75 and 10E75 plates are such that exposure for energy density below the 'toe' is greatly depressed, the effective angular range in which light diffracted from these waves is recorded on the photographic plate is even less than the angles listed above. In summary, the resultant diffraction pattern is a superposition of light wave diffracted from those plane sound waves whose wave vector deviates from the pure mode direction (as defined by the two parallel, polished crystal faces) not more than the angles as listed above. Since sound wave travels at different velocities in different directions, and the intensity of diffracted light as a function of sound wave vector is weighed by the first order Bessel function, the resultant first order positive and negative intensity patterns show disparity with respect to each other. However, the maximum error in absolute velocity measurement as determined by the distance measurement between the two spots from matching of either the top or the bottom of the two density profiles will be

Table 2

Experimental data for determination of $V_p[001]$ *and its temperature dependence*

Photographic plate designation	Vacuum gauge reading (μm)	Temperature (°C)	Transducer driving frequency (MHz)	Micro-densitometer table angle reading (Degree)	Spot separation (cm)	Ratio of transducer driving frequency and spot separation (MHz/cm)
D–2	130	20·29	28·87804	21·75	1·0628	27·171
					1·0623	27·183
D–3	120	20·34	28·87804	21·75	1·0624	27·182
					1·0619	27·195
D–5	130	20·49	29·37592	21·75	1·0803	27·193
					1·0797	27·208
D–6	150	21·67	29·37592	21·75	1·0796	27·210
					1·0802	27·196
D–7	100	20·07	29·37592	21·75	1·0805	27·188
					1·0809	27·177
D–8	150	57·08	29·34020	21·75	1·0805	27·155
					1·0812	27·136
D–9	150	59·83	29·34020	21·75	1·0806	27·152
					1·0820	27·117
D–10	150	80·64	29·31250	21·75	1·0807	27·125
					1·0801	27·139
D–11	150	80·09	29·31250	21·75	1·0822	27·087
					1·0813	27·110
D–12	175	119·33	29·26488	21·70	1·0806	27·083
					1·0796	27·108
D–13	175	120·50	29·26488	21·70	1·0805	27·084
					1·0799	27·099
D–14	175	145·83	29·23100	21·60	1·0792	27·087
					1·0803	27·059
D–15	180	146·80	29·23100	21·60	1·0801	27·063
					1·0796	27·075
D–17	90	80·93	28·81502	21·75	1·0625	27·120
					1·0622	27·128

less than the error resulting from measuring sound velocity whose propagation direction deviates from the pure mode direction by angles as listed above.

The data interpreted as described above are listed in Tables 2–5. Each table provides data for velocity measurement as a function of temperature of a pure mode. There are two spot separation readings for each photographic plate. The first reading is the separation when matching the top part of the two profiles and the second reading is the separation when matching bottom part of the two profiles. The first reading is neither consistently greater nor less than the second. It depends rather on the detailed excitation of off-pure mode plane waves. In computing the spot separation, the distance between the fixed markers is taken as the calibrated distance shown on the stage micrometer. Any error in this distance affects only the absolute velocity but not the temperature dependence of velocity measurements.

The errors discussed in the measurement of the distance between the two spots on the photographic plates by the microdensitometer read-out are:

(1) Error due to microdensitometer and stage micrometer misalignment. This is about $\sim 0{\cdot}1$ μm.

(2) Pencil marker and recorder pen trace thickness on the microdensitometer read-out chart. This error is less than 1 μm.

(3) Reproducibility of microdensitometer read-out, which is within $2{\cdot}5$ μm.

Table 3

Experimental data for determination of $V_s[001]$ *and its temperature dependence*

Photographic plate designation	Vacuum gauge reading (μm)	Temperature (°C)	Transducer driving frequency (MHz)	Micro-densitometer table angle reading (Degree)	Spot separation (cm)	Ratio of transducer driving frequency and spot separation (MHz/cm)
E-2	130	21·81	30·95130	22·60	1·5398	20·101
					1·5391	20·109
E-4	140	21·92	30·95130	22·60	1·5391	20·111
					1·5388	20·115
E-5	115	21·95	30·95130	22·60	1·5400	20·099
					1·5395	20·105
E-6	105	21·59	30·95130	22·60	1·5386	20·116
					1·5390	20·111
E-8	110	49·22	30·92020	22·40	1·5381	20·102
					1·5378	20·107
E-9	120	49·37	30·92020	22·60	1·5384	20·099
					1·5377	20·108
E-11	125	80·44	30·89004	22·60	1·5377	20·089
					1·5374	20·092
E-12	100	80·96	30·89004	22·60	1·5374	20·093
					1·5369	20·099
E-13	100	80·81	30·89004	22·40	1·5380	20·084
					1·5376	20·089
E-14	130	120·90	30·83805	22·40	1·5375	20·057
					1·5380	20·051
E-16	130	118·91	30·84604	22·50	1·5366	20·075
					1·5372	20·066
E-17	100	118·89	30·84604	22·40	1·5392	20·041
					1·5377	20·060
E-19	150	145·08	30·81604	22·60	1·5353	20·071
					1·5369	20·051
E-20	130	146·17	30·81604	22·50	1·5359	20·064
					1·5364	20·057

(4) The error involved when the direction defined by the two spots, relative to the photographic plate bottom edge, fluctuates from plate to plate. This error is typically one order of magnitude smaller than and at most one-fifth of the uncertainty in profile matching.

(5) Error involved in profile matching, on the average 5 μm. This is the major contributing factor in experimental uncertainty.

Note also in Table 2, D-2, D-4, D-5, D-6 and D-7 all measure the same velocity at room temperature, only that the D-5, D-6, D-7 measurements have one more half-wavelength inside the sample than the D-2, D-4 measurements. Also in Table 3, E-14, E-16, E-17 all measure the velocity at nearly the same temperature, but E-14 has a slightly different transducer driving frequency than E-16 and E-17. This is also the case in Table 4 between F-1, F-2, and F-6. These variations are used to check whether the present method would depend on the number of half wavelengths inside the sample, or the selection of transducer driving frequency. From the readings of the ratio of transducer driving frequency and spot separation as listed in Tables 2–5, these factors do not show any effect within the experimental error. Figs 11–14 are plots of the ratio of transducer driving frequency and spot separation *vs* temperature constructed from Tables 2–5, respectively. In these figures the short end of each error bar indicates density profile matching by top, while the long end indicates density profile matching by bottom.

Table 4

Experimental data for determination of $V_p[110]$ *and its temperature dependence*

Photographic plate designation	Vacuum gauge reading (μm)	Temperature (°C)	Transducer driving frequency (MHz)	Micro-densitometer table angle reading (Degree)	Spot separation (cm)	Ratio of transducer driving frequency and spot separation (MHz/cm)
F-1	120	18·50	30·96020	18·60	0·9918	31·216
					0·9927	31·188
F-2	100	18·57	30·96020	18·60	0·9921	31·208
					0·9925	31·196
F-3	110	49·95	30·94500	19·20	0·9930	31·162
					0·9927	31·173
F-4	95	49·31	30·94500	19·20	0·9927	31·171
					0·9938	31·140
F-5	100	49·04	30·94500	19·20	0·9932	31·157
					0·9926	31·177
F-6	95	17·87	30·97000	18·60	0·9927	31·199
					0·9932	31·183
F-7	120	78·46	30·91620	19·20	0·9939	31·105
					0·9930	31·135
F-8	130	79·13	30·91620	19·20	0·9922	31·160
					0·9927	31·144
F-10	130	113·53	30·88058	19·20	0·9925	31·114
					0·9929	31·102
F-11	140	113·49	30·88058	19·20	0·9926	31·112
					0·9928	31·104
F-12	150	145·98	30·84830	18·60	0·9929	31·069
					0·9934	31·053
F-13	150	147·87	30·84830	18·60	0·9924	31·086
					0·9929	31·070

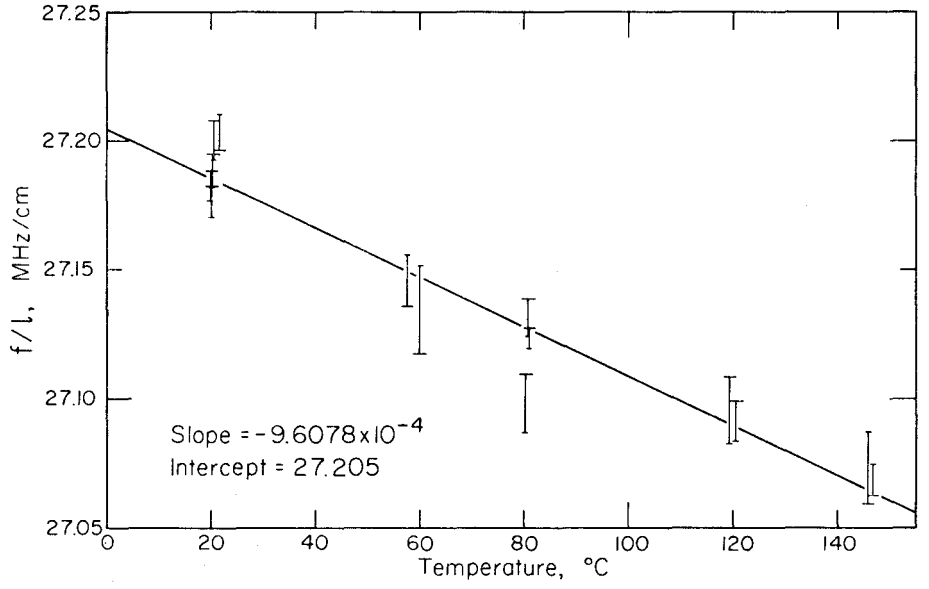

FIG. 11. Ratio of transducer driving frequency and spot separation *vs* temperature for $V_p[001]$ measurements. The short end of each error bar indicates density profile matching by top. The long end indicates density profile matching by bottom.

Table 5

Experimental data for determination of $V_s[110]$ $(P//[1\bar{1}0])$ *and its temperature dependence*

Photographic plate designation	Vacuum gauge reading (μm)	Temperature (°C)	Transducer driving frequency (MHz)	Micro-densitometer table angle reading (Degree)	Spot separation (cm)	Ratio of transducer driving frequency and spot separation (MHz/cm)
G-4	140	17·09	31·10572	20·40	2·4128	12·892
					2·4136	12·888
G-5	130	16·37	31·10572	20·40	2·4134	12·889
					2·4139	12·886
G-6	120	48·12	31·05112	20·40	2·4140	12·863
					2·4144	12·861
G-7	140	47·81	31·05112	20·40	2·4136	12·865
					2·4142	12·862
G-8	110	48·29	31·05112	20·40	2·4156	12·855
					2·4149	12·858
G-9	90	80·62	30·99005	20·40	2·4119	12·849
					2·4116	12·851
G-10	100	80·40	30·99005	20·40	2·4141	12·837
					2·4133	12·841
G-11	100	119·02	30·93251	20·40	2·4125	12·822
					2·4117	12·826
G-12	85	118·90	30·93251	20·60	2·4110	12·830
					2·4111	12·829
G-13	115	149·05	30·87503	20·60	2·4128	12·796
					2·4132	12·795
G-14	120	149·11	30·87503	20·60	2·4122	12·800
					2·4120	12·801
G-15	110	149·29	30·87503	20·60	2·4117	12·802
					2·4122	12·799

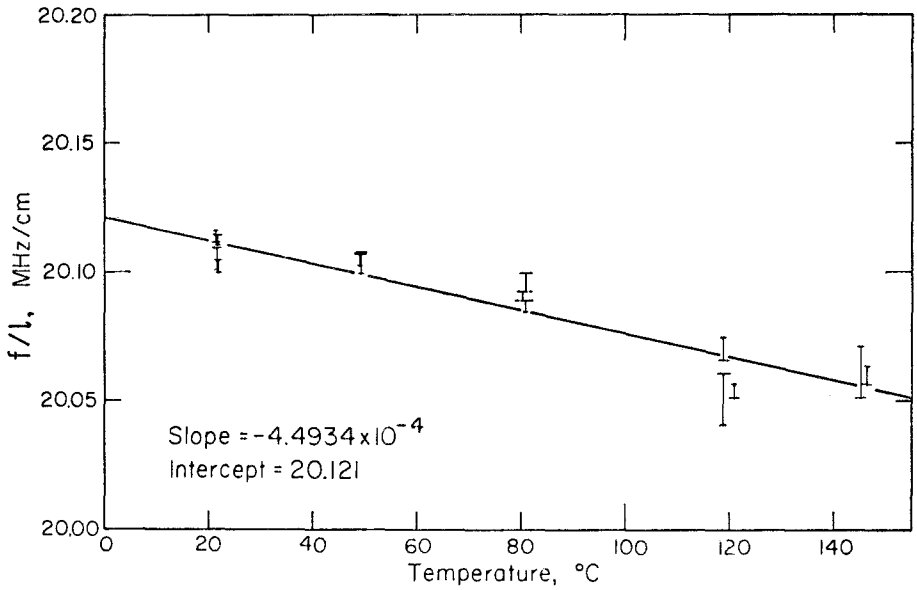

FIG. 12. Ratio of transducer driving frequency and spot separation *vs* temperature for $V_s[001]$ measurements. The short end of each error bar indicates density profile matching by top. The long end indicates density profile matching by bottom.

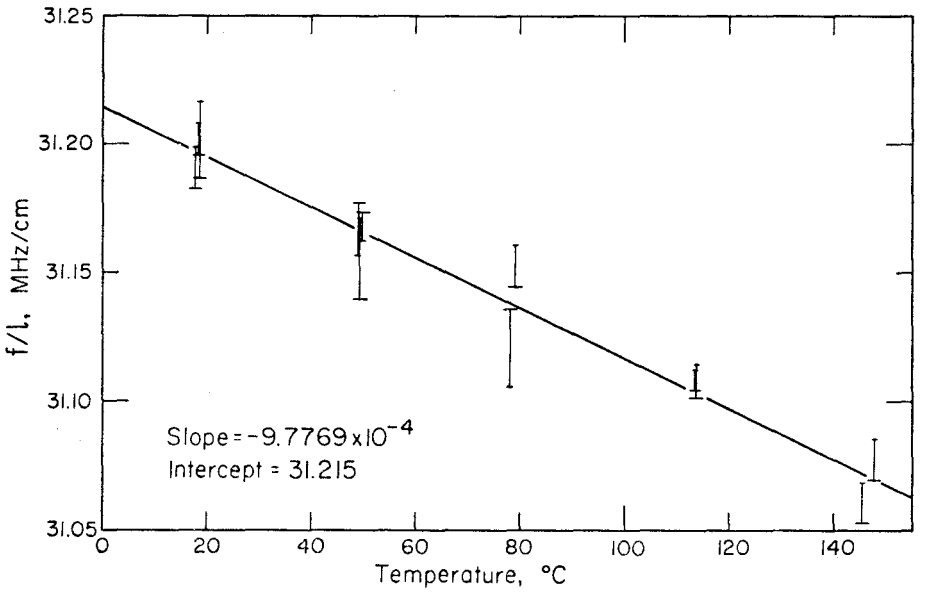

FIG. 13. Ratio of transducer driving frequency and spot separation *vs* temperature for V_p[110] measurements. The short end of each error bar indicates density profile matching by top. The long end indicates density profile matching by bottom.

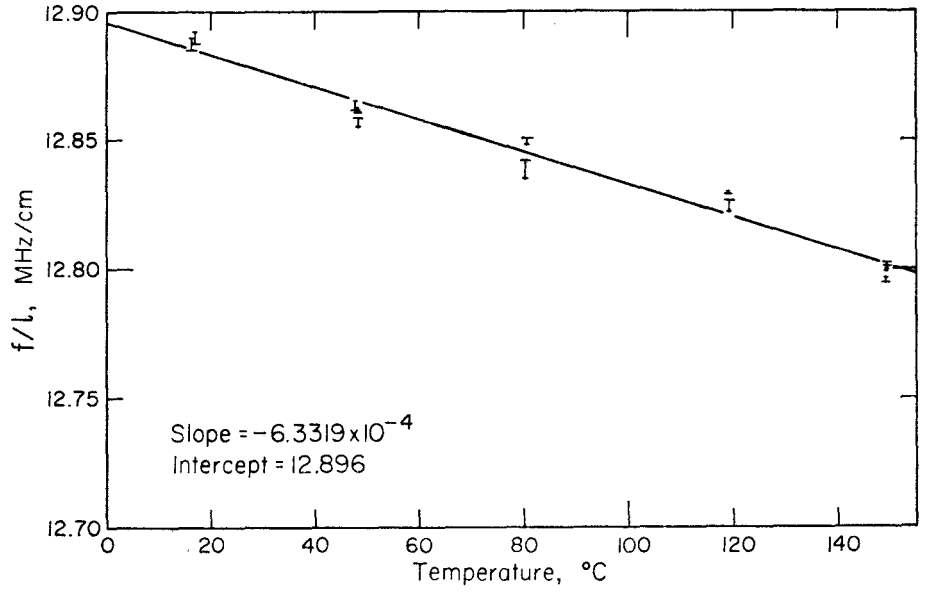

FIG. 14. Ratio of transducer driving frequency and spot separation *vs* temperature for V_s[110] (P//[1$\bar{1}$0]) measurements. The short end of each error bar indicates density profile matching by top. The long end indicates density profile matching by bottom.

A linear temperature dependence is fit to the quantity f/l in Figs 11–14 by a least-square method. The method is to minimize the sum of the distance from centre of each error bar to the straight line squared. The intercept at 0 °C and slope of each least-square fit straight line are labelled in each figure.

The standard deviation of the parameters of any least-square fit scheme depends on the meaning of the error of each individual data point. For example, if the error bar represents one standard deviation of a Gaussian distribution from repeated measurements at the same given value of the independent variable, the standard deviation of the parameters in the least-square fit can be calculated, for example, according to Whittaker & Robinson (1944). The error bars in the present case, as explained earlier, however, represent the latitude in the matching of the two density profiles, and the probability distribution inside the error bars is not necessarily Gaussian. The assignment of standard deviation to the parameters is therefore difficult. Instead, a measure of uncertainty in these parameters is assigned by a consistency check which will be discussed later.

Before computing the velocity and its temperature dependence from these results, two more possible sources of error must be considered. The first is error in temperature measurement. As stated in Section 3.1, the temperatures are measured at two sites located at diagonally opposite corners of the sample. Each temperature reading listed in Tables 2–5 is an average of the temperatures at the two thermocouple sites. At room temperature the two thermocouples give identical readings. At higher temperatures the two readings differ. This difference is ~ 5 °C at 150 °C. The cause of this difference is that the centre of the sample holder assembly deviates slightly from the furnace centre. This means that the temperature reading is uncertain to $\pm 3{\cdot}2$ °C at 150 °C. (Assuming the thermocouple measures to an absolute accuracy of 1 °C.) Since room temperature is ~ 20 °C for all measurements, this would introduce an error of $\pm 3{\cdot}2°/130° = \pm 3$ per cent to the slopes in Figs 11–14. Another possible source of error comes from the lensing effect at the exit sample face if a radial temperature gradient exists in the furnace. A separate test is conducted to determine the upper limit of this radial thermal gradient. Fused silica (1 cm × 1 cm × 1 cm) is placed inside the furnace in place of the spinel sample. A third thermocouple is pasted at the centre of the exit face (face toward the shutter) by Sauereisen cement. At ~ 100 °C the three thermocouple readings are 1·466 mV (thermocouple at one corner of the exit face), 1·660 mV (thermocouple at the diagonally opposite corner) and 1·256 mV (thermocouple at centre of the exit face). Since 0·1 mV corresponds to 2·22 °C and since the third thermocouple placed inside the tubular furnace provides a

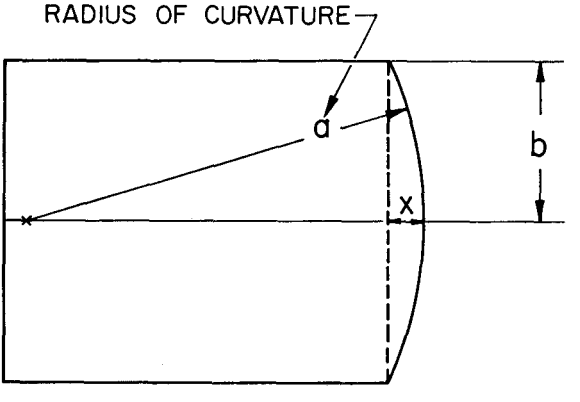

FIG. 15. Illustration of lensing effect of crystal face due to temperature gradient.

conduction path between high temperature region of the furnace and low temperature region outside the furnace (this heat conduction path is absent during the optical measurement), the maximum radial temperature difference across the sample during the optical measurement is estimated to be

$$4{\cdot}44\,^{\circ}\mathrm{C} \times \frac{3{\cdot}25}{22{\cdot}65} = 0{\cdot}63\,^{\circ}\mathrm{C} \text{ at } 100\,^{\circ}\mathrm{C}.$$

3·25/22·65 is the ratio of thermal conductivity of fused silica and spinel (Horai 1971). The lensing effect of the exit face can be estimated as follows. Refer to Fig. 15, $x = 6{\cdot}93 \times 10^{-6}\,\Delta T$, where $6{\cdot}93 \times 10^{-6}/K$ is the linear thermal expansion coefficient of spinel (Rigby, Lovell & Green 1946), $b = 0{\cdot}8$ cm is the distance between corner thermocouple and centre thermocouple. The curvature a is given by $a = b^2/2x = 0{\cdot}64/(2 \times 6{\cdot}93 \times 10^{-6}\,\Delta T)$. The change in diffraction angle due to lensing effect is then

$$\Delta\theta = (n_{\text{spinel}} - 1)\frac{r}{a} = 0{\cdot}719\frac{r}{a} = 15{\cdot}6 \times 10^{-6}\, r \Delta T.$$

The corresponding change in spot separation on the photographic plate is $\Delta l = L\Delta\theta = 15{\cdot}6 \times 10^{-6} r \Delta T L$, where L is the distance between sample and photographic plate. Take $V_s[001]$ measurement, for example,

$$r = (\lambda_0 \times 1{\cdot}179/\Lambda)\text{ cm}$$
$$= (0{\cdot}6328 \times 10^{-4} \times 30{\cdot}85 \times 10^{6} \times 1{\cdot}179/6{\cdot}57 \times 10^{5})\text{ cm} = 3{\cdot}50 \times 10^{-3}\text{ cm},$$
$$L = 257{\cdot}7\text{ cm},$$
$$\Delta l = 1{\cdot}41 \times 10^{-5}\,\Delta T\text{ cm/°C},$$
$$l = 1{\cdot}54\text{ cm},$$
$$\Delta l/l = 0{\cdot}91 \times 10^{-5}\,\Delta T.$$

With

$$\frac{d(f/l)/dT}{(f/l)} = 0{\cdot}22 \times 10^{-4}\,^{\circ}\mathrm{C},$$

the lensing effect introduces an error of

$$\frac{0{\cdot}91 \times 10^{-5}}{0{\cdot}22 \times 10^{-4}}\,\frac{0{\cdot}63\,^{\circ}\mathrm{C}}{80\,^{\circ}\mathrm{C}} = 0{\cdot}3 \text{ per cent}$$

between room temperature and 100 °C. This is negligible in comparison with other sources of error.

The velocity and its temperature dependence are computed from the value f/l by the equations

$$V = f\Lambda = \left(L + \frac{t}{2n_{\text{spinel}}}\right)2\lambda_0\left(\frac{f}{l}\right) \tag{27}$$

where

t: sample thickness

λ_0: laser wavelength in vacuum, $\lambda_0 = 0{\cdot}6328\ \mu$m

$$\left(\frac{\partial V}{\partial T}\right)_p = \left(L + \frac{t}{2n_{\text{spinel}}}\right)2\lambda_0\left(\frac{\partial(f/l)}{\partial T}\right)_p. \tag{28}$$

The values of velocity of the four pure modes at 25 °C and their temperature derivatives, together with values of L and t are listed in Table 6. The four pure mode velocities are given by

$$\left.\begin{aligned} V_1 &\equiv V_p[001] = \sqrt{C^s_{11}/\rho}, \\ V_2 &\equiv V_s[001] = \sqrt{C^s_{44}/\rho} \\ V_3 &\equiv V_p[110] = \sqrt{(C^s_{11}+C^s_{12}+2C^s_{44})/2\rho} \\ V_4 &\equiv V_s[110](P//[1\bar{1}0]) = \sqrt{(C^s_{11}-C^s_{12})/2\rho} \end{aligned}\right\} \tag{29}$$

where C^s_{11}, C^s_{12} and C^s_{44} are the three adiabatic elastic constants of spinel and ρ is its density. It follows from (29) that

$$V_1^2+V_2^2 = V_3^2+V_4^2 \tag{30}$$

and

$$V_1\left(\frac{\partial V_1}{\partial T}\right)_p+V_2\left(\frac{\partial V_2}{\partial T}\right)_p = V_3\left(\frac{\partial V_3}{\partial T}\right)_p+V_4\left(\frac{\partial V_4}{\partial T}\right)_p. \tag{31}$$

These two equations serve for consistency check of the experimental results. From Table 6, $V_1^2+V_2^2 = 121{\cdot}77\,\mathrm{km^2\,s^{-2}}$, and $V_3^2+V_4^2 = 121{\cdot}74\,\mathrm{km^2\,s^{-2}}$. The agreement is within 0·03 per cent. The reason that the consistency check shows a closer agreement than the individual errors in velocity (as listed in Table 6) would indicate that the major contribution to the individual errors in Table 6 comes from the systematic calibration error of AO 1400 stage micrometer which contributes only to the second order in error in a consistency check. For the consistency check on temperature derivatives of velocity, Table 6 gives

$$V_1\left(\frac{\partial V_1}{\partial T}\right)_p+V_2\left(\frac{\partial V_2}{\partial T}\right)_p = -37{\cdot}50\times10^{-4}\,\mathrm{km^2\,s^{-2}\,K^{-1}}$$

and

$$V_3\left(\frac{\partial V_3}{\partial T}\right)_p+V_4\left(\frac{\partial V_4}{\partial T}\right)_p = -41{\cdot}36\times10^{-4}\,\mathrm{km^2\,s^{-2}\,K^{-1}}.$$

The disagreement is 9·6 per cent. It has been remarked previously that it is difficult in the present experiment to ascertain the standard deviation of the temperature derivatives from individual error bars. The consistency check provides an alternative way to assign a measure of experimental uncertainty to these temperature derivatives. The disagreement between

$$V_1\left(\frac{\partial V_1}{\partial T}\right)_p+V_2\left(\frac{\partial V_2}{\partial T}\right)_p \quad \text{and} \quad V_3\left(\frac{\partial V_3}{\partial T}\right)_p+V_4\left(\frac{\partial V_4}{\partial T}\right)_p$$

is 9·6 per cent. Since the absolute value of velocities V_1, V_2, V_3 and V_4 are accurate to better than 0·1 per cent, the disagreement can be considered to arise from the velocity derivatives alone. Note also that in Figs 11–14 the four temperature derivatives have different errors. A strategy to assign weighing factors to these temperature derivatives is as follows. Assume that the error involved in profile matching is the same for all four velocity measurements. A check on the spot separation column in Tables 2–5 indicates this to be a good approximation. Denote this matching error by ε. The percentage error in slope of the quantity f/l *vs* T in Figs 11–14 (which is also the percentage error of $(\partial V/\partial T)_p$) is then

$$\left|(f/l)\frac{\varepsilon}{l}\Big/\left[\left(\frac{f}{l}\right)_{150°C}-\left(\frac{f}{l}\right)_{20°C}\right]\right|.$$

Table 6

Ultrasonic velocities and their isobaric temperature derivatives of spinel at 25 °C

Mode	Velocity at at 25 °C, V ($km\,s^{-1}$)	Isobaric temperature derivative, $(\partial V/\partial T)_p$ ($10^{-4}\,km\,s^{-1}\,K$)	Distance between sample and plate, L (cm)	Sample thickness at 25 °C, t (cm)
L//[001]	8·869	−3·14	257·46	1·1793
	±0·013	±0·13(±4·2%)	±0·03	±0·0003
T//[001]	6·5666	−1·47	257·67	1·1793
	±0·0055	±0·10(±6·6%)	±0·03	±0·0003
L//[110]	10·199	−3·20	258·36	0·8923
	±0·011	±0·15(±4·7%)	±0·03	±0·0003
T//[1$\bar{1}$0]	4·2101	−2·07	258·02	0·8923
(P//[1$\bar{1}$0])	±0·0043	±0·06(±3·0%)	±0·03	±0·0003

Note:

(1) The error in the absolute velocity includes American Optical Corporation A01400 stage micrometer calibration error, photographic density profile matching error, sample thickness measurement error, and error in length measurement between sample and photographic plate.

(2) The uncertainties in isobaric temperature derivatives of velocity are assigned from consistency check.

From this expression, the percentage error for $(\partial V_1/\partial T)_p$ is calculated to be 217ε; that for $(\partial V_2/\partial T)_p$ 342ε; for $(\partial V_3/\partial T)_p$ 245ε; and for $(\partial V_4/\partial T)_p$ 156ε. Let $\{(217)^2+(342)^2+(245)^2+(156)^2\}^{\frac{1}{2}}\varepsilon = \pm 9{\cdot}6$ per cent. Solving for ε, the resulting percentage errors for the four velocity temperature derivatives are ±4·2 per cent for $(\partial V_1/\partial T)_p$, ±6·6 per cent for $(\partial V_2/\partial T)_p$, ±4·7 per cent for $(\partial V_3/\partial T)_p$, and ±3·0 per cent for $(\partial V_4/\partial T)_p$. The range of temperature derivatives of velocity allowed by the uncertainty of *individual* measurements as shown in Figs 11–14 are:

$$\left(\frac{\partial V_1}{\partial T}\right)_p = \begin{pmatrix} -2{\cdot}18 \\ -3{\cdot}82 \end{pmatrix} \times 10^{-4}\,km\,s^{-1}\,K^{-1},$$

$$\left(\frac{\partial V_2}{\partial T}\right)_p = \begin{pmatrix} -0{\cdot}82 \\ -1{\cdot}69 \end{pmatrix} \times 10^{-4}\,km\,s^{-1}\,K^{-1},$$

$$\left(\frac{\partial V_3}{\partial T}\right)_p = \begin{pmatrix} -2{\cdot}49 \\ -4{\cdot}12 \end{pmatrix} \times 10^{-4}\,km\,s^{-1}\,K^{-1},$$

$$\left(\frac{\partial V_4}{\partial T}\right)_p = \begin{pmatrix} -2{\cdot}05 \\ -2{\cdot}41 \end{pmatrix} \times 10^{-4}\,km\,s^{-1}\,K^{-1}.$$

The experimental uncertainties deduced from the consistency check are certainly allowed within these ranges.

4. Results and comparison with other experiments

The values of velocity corresponding to the four pure modes at 25 °C and their temperature derivatives are listed in Table 6. The adiabatic elastic constants C^s_{11}, C^s_{12}, C^s_{44} and the adiabatic bulk modulus $K^s = \frac{1}{3}(C^s_{11}+2C^s_{12})$ of spinel can be calculated from (29) with $\rho = 3{\cdot}5784\,g\,cm^{-3}$ at 25 °C. The temperature derivatives of the elastic constants are calculated from

$$\left(\frac{\partial C_i^s}{\partial T}\right)_p = \rho V_i\left[2\left(\frac{\partial V_i}{\partial T}\right)_p - 3\alpha V_i\right] \qquad i = 1, 2, 3, 4 \tag{32}$$

Table 7

Adiabatic elastic constants, bulk modulus, and their isobaric temperature derivatives

C_{11}^s	C_{44}^s	C_{12}^s	$K_s = \left(\frac{C_{11}^s + 2C_{12}^s}{3}\right)$	$\left(\frac{\partial C_{11}^s}{\partial T}\right)_p$	$\left(\frac{\partial C_{44}^s}{\partial T}\right)_p$	$\left(\frac{\partial C_{12}^s}{\partial T}\right)_p$	$\left(\frac{\partial K_s}{\partial T}\right)_p$	
(kb)	(kb)	(kb)	(kb)	(kb/K)	(kb/K)	(kb/K)	(kb/K)	(10^{-6}/K)
2814	1543	1546*	1969*	−0·258	−0·101	−0·107*	−0·157*	6·93†
±8	±3	±9	±6	±0·018	±0·01	±0·019	±0·014	
		1544‡	1967‡			−0·161‡	−0·193‡	
		±19	±13			±0·052	±0·035	

* Values calculated from V_s//[110](P//[1$\bar{1}$0]) measurement.

† Linear thermal expansion coefficient from Rigby *et al.* (1946).

‡ Values calculated from V_p^s//[110] measurement.

where α is linear thermal expansion coefficient and

$$\left.\begin{aligned} &C_1^s \equiv C_{11}^s, \quad C_2^s \equiv C_{44}^s, \quad C_3^s \equiv \tfrac{1}{2}(C_{11}^s + C_{12}^s + 2C_{44}^s) \\ &\text{and} \\ &C_4^s \equiv \tfrac{1}{2}(C_{11}^s - C_{12}^s). \end{aligned}\right\} \tag{33}$$

The temperature derivative of the adiabatic bulk modulus is calculated from

$$\left(\frac{\partial K^s}{\partial T}\right)_p = \frac{1}{3}\left[\left(\frac{\partial C_{11}^s}{\partial T}\right)_p + 2\left(\frac{\partial C_{12}^s}{\partial T}\right)_p\right]. \tag{34}$$

These values are listed in Table 7.

In order to apply the temperature dependence data of single-crystal elastic constants to the interpretation of Earth's mantle composition, the data must be put into several different forms and utilized in several calculations. The Debye temperature of single-crystal spinel can be calculated from elastic constants according to methods summarized by Alers (1965). The calculated value is $\theta_{\text{spinel}} = 883\,^\circ\text{K}$ using de Launay's formula. The thermal Grüneisen's parameters are calculated to be

$$\gamma_{\text{th}} = \frac{\beta K_s}{\beta C_p} = 6{\cdot}93 \times 3 \times 10^{-6} \times 1969 \times 10^9/(3{\cdot}5784 \times 0{\cdot}815 \times 10^7) = 1{\cdot}40 \tag{35}$$

for the first Grüneisen parameter, and

$$\delta_{\text{th}} = -\frac{1}{\beta K_s}\left(\frac{\partial K_s}{\partial T}\right)_p = 0{\cdot}157/(6{\cdot}93 \times 10^{-6} \times 1969 \times 3) = 3{\cdot}84 \tag{36}$$

for the Anderson–Grüneisen parameter, where β is volume thermal expansion coefficient and $C_p = 0{\cdot}815\ \text{J g}^{-1}\ \text{K}^{-1}$ is the specific heat at constant pressure with the value given by Bonnickson (1955). The isothermal bulk modulus is given by

$$K_T = K_s(1 + T\beta\gamma_{\text{th}}) \tag{37}$$

and its temperature derivative is, on differentiation of (37), given by

$$\left(\frac{\partial K_T}{\partial T}\right)_p = \left(\frac{\partial K_s}{\partial T}\right)_p (1 + T\beta\gamma_{\text{th}})^{-1} - K_s\gamma_{\text{th}}[1 + T\beta\gamma_{\text{th}}]^{-2}\left[\beta + T\left(\frac{\partial \beta}{\partial T}\right)_p\right] \tag{38}$$

$(\partial\beta/\partial T)_p$ is measured to be $1{\cdot}20 \times 10^{-8}\ \text{K}^{-1}$ by Rigby *et al.* (1946). Anderson (1966)

showed that for oxide compounds

$$\left(\frac{\partial K_s}{\partial T}\right)_p = -\frac{\gamma_{th}\delta_{th}}{V_0} C_v \tag{39}$$

where V_0 is the volume at absolute zero.

Anderson's derivation assumes that thermal Grüneisen parameters are identical to the mode γ's in lattice dynamics and that the Grüneisen parameters are temperature independent. Chang & Barsch (1973) concluded that for single-crystal spinel, the first assumption is bad. Based on Achar & Barsch (1971) and Barsch & Achar (1972), Chang & Barsch concluded that the second assumption in Anderson's derivation is valid for $T \cong \theta/2$. In short, (39) holds in the form

$$\left(\frac{\partial K_s}{\partial T}\right)_p \propto C_v \quad \text{for} \quad T \gtrsim \frac{\theta}{2} \tag{40}$$

independent of assumptions regarding Grüneisen parameters. Since

$$C_v = 3R[4D(x) - 3x(e^x - 1)^{-1}] \qquad x = \theta/T \tag{41}$$

where $D(x)$ is the Debye function, and $C_v = 3R = 5{\cdot}961\ \text{cal mol}^{-1}\,\text{K}^{-1}$ at high temperatures ($T \gg \theta$), (40), (41) can be used to calculate the temperature dependence of bulk modulus at high temperatures. From Table 7,

$$\left(\frac{\partial K_s}{\partial T}\right)_p = -0{\cdot}157 \pm 0{\cdot}014\ \text{kb K}^{-1} \quad \text{at} \quad T = \left(\frac{293+423}{2}\right) \pm 65\ \text{K} = (358 \pm 65)\text{K},$$

$\theta/T = 2{\cdot}47 \pm 0{\cdot}45$, $C_v(\theta/T) = 4{\cdot}485 \pm 0{\cdot}435\ \text{cal mol}^{-1}\,\text{K}^{-1}$. From (40), (41)

$$\left(\frac{\partial K_s}{\partial T}\right) = -0{\cdot}209 \pm 0{\cdot}028\ \text{kb K}^{-1} \quad \text{for} \quad T \gg \theta. \tag{42}$$

The bulk modulus of spinel is identical for single crystal and its polycrystalline aggregates. The shear modulus for a polycrystalline aggregate can be expressed in terms of Voigt, Reuss and Hill averages. These and their temperature derivatives are calculated according to expressions given by Chung (1967):

$$\left.\begin{aligned}
\mu_v &= \tfrac{1}{5}(C^s_{11} - C^s_{12} + 3C^s_{44}) = (1179 \pm 3)\ \text{kb} \\
\mu_R &= 5(C^s_{11} - C^s_{12})C^s_{44}/[3(C^s_{11} - C^s_{12}) + 4C^s_{44}] = (981 \pm 10)\ \text{kb} \\
\mu_{VRH} &= \tfrac{1}{2}(\mu_v + \mu_R) = (1080 \pm 5)\ \text{kb} \\
\left(\frac{\partial \mu_v}{\partial T}\right)_p &= \frac{1}{5}\left(\frac{\partial C^s_{11}}{\partial T} - \frac{\partial C^s_{12}}{\partial T} + 3\frac{\partial C^s_{44}}{\partial T}\right)_p = (-0{\cdot}091 \pm 0{\cdot}008)\ \text{kb K}^{-1} \\
\left(\frac{\partial \mu_R}{\partial T}\right)_p &= \frac{4}{5}\left(\frac{\mu_R}{C^s_{11} - C^s_{12}}\right)^2\left(\frac{\partial C^s_{11}}{\partial T} - \frac{\partial C^s_{12}}{\partial T}\right)_p + \frac{3}{5}\left(\frac{\mu_R}{C^s_{44}}\right)^2\left(\frac{\partial C^s_{44}}{\partial T}\right)_p \\
&= -0{\cdot}097 \pm 0{\cdot}013\ \text{kb K}^{-1} \\
\left(\frac{\partial \mu_{VRH}}{\partial T}\right)_p &= \frac{1}{2}\left(\frac{\partial \mu_v}{\partial T}\right)_p + \frac{1}{2}\left(\frac{\partial \mu_R}{\partial T}\right)_p = -0{\cdot}094 \pm 0{\cdot}008\ \text{kb K}^{-1}.
\end{aligned}\right\} \tag{43}$$

The shear modulus obeys an equation similar to (40) only if Poisson's ratio is independent of temperature (Anderson 1966). These various temperature derivatives given above can then be applied to density and velocity calculations inside Earth's mantle using various averaging schemes and extrapolation based on temperature

Table 8

Ultrasonic sound velocities (in km s^{-1}) at 25 °C and their first temperature derivatives (in 10^{-4} km s^{-1} K^{-1}) of single-crystal spinel

	V_1 $\sqrt{\left(\frac{C_{11}^s}{\rho}\right)}$	V_2 $\sqrt{\left(\frac{C_{44}^s}{\rho}\right)}$	V_3 $\sqrt{\left(\frac{C_{11}^s+C_{12}^s+2C_{44}^s}{2\rho}\right)}$	V_4 $\sqrt{\left(\frac{C_{11}^s-C_{12}^s}{2\rho}\right)}$	$\sqrt{\left(\frac{K^s+\frac{4}{3}\mu_{VRH}}{\rho}\right)}$	$\sqrt{\left(\frac{\mu_{VRH}}{\rho}\right)}$	Specimen, author and technique	Temperature range K
M	8·869 ±0·013	6·5666 ±0·0055	10·199 ±0·011	4·2101 ±0·0043	9·760 ±0·013	5·494 ±0·013	$MgO.Al_2O_3$ Present	293–423 K
$\left(\frac{\partial M}{\partial T}\right)_p$	−3·14 ±0·13	−1·47 ±0·10	−3·20 ±0·15	−2·07 ±0·06	−3·77 ±0·43	−1·82 ±0·20		
M	8·8850 ±0·0088	6·5747 ±0·004	10·2149 ±0·0057	4·2220 ±0·012	—	—	$MgO.Al_2O_3$ Chang & Barsch (1973)	308–328 K
$\left(\frac{\partial M}{\partial T}\right)_p$	−3·20 ±0·03	−1·18 ±0·04	−2·62 ±0·03	−2·25 ±0·08	—	—	Pulse superposition	
M	8·8790 ±0·0016	6·5645 ±0·0021	10·2070 ±0·0017	4·2126 ±0·0024	—	—	$MgO.Al_2O_3$ O'Connel & Graham (1971)	300–400 K
$\left(\frac{\partial M}{\partial T}\right)_p$	−3·956 ±0·032	−2·213 ±0·021	−3·62 ±0·41	−0·743 ±0·010	—	—	Ultrasonic inteferometry	Two end points only

Note:

The values of O'Connell & Graham are calculated from $C_{11}^s = 2821 \pm 1$ kb, $C_{12}^s = 1551 \pm 1$ kb, $C_{44}^s = 1542 \pm 1$ kb; $(\partial C_{11}^s/\partial T)_p = -0{\cdot}31 \pm 0{\cdot}002$ kb/K, $(\partial C_{44}^s/\partial T)_p = -0{\cdot}136 \pm 0{\cdot}001$ kb/K, $[\partial(C_{11}^s+C_{12}^s+2C_{44}^s)/2\partial T]_p = -0{\cdot}342 \pm 0{\cdot}03$ kb/K, and $[\partial(C_{11}^s-C_{12}^s)/2\partial T]_p = -0{\cdot}0544 \pm 0{\cdot}0003$ kb/K, $\rho = 3{\cdot}5783$ g cm^{-3}, and linear thermal expansion coefficient $\alpha = 6{\cdot}93 \times 10^{-6}$/K (Rigby *et al.* 1946).

dependent equation of state. The significance of various averaging schemes are discussed, for example, in Kumazawa (1969) and in Thomsen (1972a, b). One example of discussing the composition of Earth's upper mantle in terms of temperature and pressure dependence of elasticity is given by Graham (1970).

The elastic constants of stoichiometric single-crystal spinel have been measured by Chang & Barsch (1973), O'Connell & Graham (1971) and Lewis (1966). The elastic constants of non-stoichiometric spinel have been measured by Schreiber ($MgO.2.61\ Al_2O_3$, Anderson *et al.* 1968), and by Verma ($MgO.3.5\ Al_2O_3$, 1960). Chang & Barsch (1973), O'Connell & Graham (1971), and Schreiber (Anderson *et al.* 1968) also measured their pressure and temperature dependence. The results of the three most recent measurements together with their methods are listed in Table 8. They merit a comparison, since all of them are obtained from single-crystal samples grown by the Crystal Products Division of Union Carbide Corporation, and two of them (the present work and that of O'Connell & Graham 1971) are obtained from the same sample. It is seen from Table 8 that the absolute velocity measurements agree within experimental error but the temperature dependence of velocities generally disagrees among the three measurements. Compare the values of present work and those of Chang & Barsch (1973). The value $(\partial V_1/\partial T)_p$ of Chang & Barsch agrees within experimental uncertainty (as assigned by the consistency check) with the present measurement. Their values of $(\partial V_2/\partial T)_p$, $(\partial V_3/\partial T)_p$, and $(\partial V_4/\partial T)_p$ lie outside of the experimental uncertainty as assigned by the consistency check, but lie within the range of values allowed by the individual measurements of the present experiment as discussed in Section 3.3. Comparing the values of the present work and those obtained by O'Connell & Graham (1971), their $(\partial V_3/\partial T)_p$ agrees within experimental uncertainty (as assigned by the consistency check) with the present measurement. However, values of $(\partial V_1/\partial T)_p$, $(\partial V_2/\partial T)_p$ and $(\partial V_4/\partial T)_p$ calculated from O'Connell & Graham's data lie outside the range of values allowed by uncertainty in individual measurements. The conclusion is that the experimental values as obtained from the present method are consistent with the measurements obtained by Chang & Barsch (1973) but disagree with those obtained by O'Connell & Graham (1971). The measurements of Chang & Barsch (1973) are based on the method of pulse superposition (McSkimin 1961; McSkimin & Andreatch 1962), and those of O'Connell & Graham are based on the method of gated double-pulse interferometry through a buffer rod (Spetzler 1970). In the pulse superposition method, the phase shifts at the sample-transducer interface must be corrected for. This correction involves the acoustical impedances of bond and transducer, their thickness, and their phase shift constants. Several difficulties which limit the accuracy of the measurement are: (1) The resonance peak of the bonded transducer is not sharp and deteriorates with temperature and pressure, which makes transducer phase shift constant difficult to determine. (2) The bond acoustic impedance changes with pressure and temperature and is generally not corrected for. Also, in the shear wave measurements, the acoustical impedance of the thin film Nonaq stopcock grease bond depends on its viscosity (Thurston 1964) but is generally unaccounted for. (3) Effects of transducer radiation pattern and side reflections. The buffer rod technique of Spetzler assumes zero phase shift at the lapped sample-buffer rod interface. Side reflections from the buffer rod and sample are not taken into consideration. Also, in picking maximum interference conditions, the frequency response of the transducer and the effect of bandwidth of the electronics, which envelope modulates the maxima conditions, are neglected in the analysis. Both methods require exact sample length determination at all temperatures and pressures. The method of light-sound scattering in the Raman–Nath region, however, is free from these corrections. Since the interaction of light and sound takes plade inside the sample and the light samples only that portion of the sound wave which lies in its path, the exact manner in which sound is coupled into the crystal is immaterial. The only error introduced by the boundaries of the sample, as

discussed in Section 3.3, is the profile distortion of the diffracted light intensities. This also limits the precision of the present method of sound velocity measurement.

In view of the different nature of experimental errors involved in the ultrasonic methods and the light-sound scattering method, and the lack of detailed studies of the errors in the ultrasonic methods, the agreement between the present measurements and those by Chang & Barsch (1973) may be fortuitous.

5. Evaluation of light-sound scattering as a method to measure temperature and pressure dependence of elastic constants

The precision of the present method can be improved appreciably if instead of standing waves, travelling waves are used as the diffraction grating. If the sample is shaped at one end in a wedge and the wedge end bounded to an absorber (usually a soft metal, which attenuates effectively ultrasound with frequencies above 20 MHz), the sound wave launched at the opposite end by the transducer is absorbed after travelling through the crystal. The acoustic wave will not feel the presence of the sides if the transducer is smaller than the sample face on which it is mounted and if the transducer frequency is high enough. This will truly be a setup to measure accurately sound propagation velocity in an infinite medium, which has not been done. With boundary effects removed, the accuracy of velocity measurement can be extended to 5×10^{-5}. The temperature dependence of sound velocities in solids can be measured to 670 °C with $LiNbO_3$ transducer and a cold-weld gold-indium bond (Sittig & Cook 1968).

An attempt has also been made by the authors to measure the pressure dependence of elastic constants of spinel with the same technique. The high pressure optical cell employed in the experiment is the one designed by Stromberg & Schock (1970). Preliminary results of this measurement showed large spurious diffraction of the laser beams by the fluctuation in index of refraction of the pressure fluid due to thermal convection within the vessel generated by heat dissipation from the transducer. However, thermal convection can be eliminated and there is no intrinsic reason that the present technique cannot be used to measure the pressure dependence of single-crystal elastic constants.

Acknowledgments

This work was supported by the National Aeronautics and Space Administration under Grant #NGL05-002-069, Sup. 5. The authors wish to thank Dr Richard MacAnally and Professor Hiroo Kanamori for some very useful discussions. A portion of this work was performed under the auspices of the US Atomic Energy Commission.

Hsi-Ping Liu and Don L. Anderson:
Seismological Laboratory,
California Institute of Technology,
Pasadena, California.

R. N. Schock:
Lawrence Livermore Laboratory,
University of California,
Livermore, California.

References

Achar, B. N. N. & Barsch, G. R., 1971. Shell model calculations of thermal expansion of alkali halides and magnesium oxide, *Phys. Status Solidi* (a), **6**, 247.

Alers, G. A., 1965. Use of sound velocity measurements in determining the Debye temperature of solids, in *Physical Acoustics*, 1–40, ed. W. P. Mason, *IIIB*, Academic Press, New York.

Anderson, D. L., Sammis, C. G. & Jordan, T. H., 1972. Composition of the mantle and core, in *The Nature of the Solid Earth*, 41–66, ed. Eugene C. Robertson, McGraw–Hill, Inc., New York.

Anderson, O. L., 1966. Derivation of Wachtman's equation for the temperature dependence of elastic moduli of oxide compounds, *Phys. Rev.*, **144**, 553.

Anderson, O. L., Schreiber, E., Lieberman, R. C. & Soga, N., 1968. Some elastic constant data on minerals relevant to geophysics, *Rev. Geophys.*, **6**, 491.

Barsch, G. R. & Achar, B. N. N., 1972. Shell model calculation of second Grüneisen parameters for alkali halides, *Am. Inst. Phys. Conf. Proc.*, **3**, 211.

Bergmann, L., 1954. *Der Ultraschall*, Hirzel, Zurich.

Bonnickson, K. R., 1955. High-temperature heat contents of aluminates of calcium and magnesium, *J. Phys. Chem.*, **59**, 220.

Chang, Z. P. & Barsch, G. R., 1973. Pressure dependence of single-crystal elastic constants and anharmonic properties of spinel, *J. geophys. Res.*, **78**, 2418.

Christensen, N. I., 1974. Compressional wave velocities in possible mantle rocks to pressure of 30 kbar, *J. geophys. Res.*, **79**, 407.

Chung, D. H., 1967. First pressure derivative of polycrystalline elastic moduli; their relation to single-crystal acoustic data and thermodynamic relations, *J. appl. Phys.*, **38**, 5104.

Debye, P. & Sears, F. W., 1932. On the scattering of light by supersonic waves, *Proc. natl. Acad. Sci.*, **18**, 409.

Dixon, R. W., 1967. Acoustic diffraction of light in anisotropic media, *J. quantum Electronics*, **QE–3**, 85.

Extermann, R. & Wannier, G., 1936. Theorie de la diffraction de la lumiére par les ultrasons, *Helv. Phys. Acta*, **9**, 520.

Frisillo, A. L. & Barsch, G. R., 1972. Measurement of single-crystal elastic constants of bronzite as a function of pressure and temperature, *J. geophys. Res.*, **77**, 6360.

Graham, E. K., 1970. Elasticity and composition of the upper mantle, *Geophys. J. R. astr. Soc.*, **20**, 285.

Graham, E. K. & Barsch, G. R., 1969. Elastic constants of single-crystal forsterite as a function of temperature and pressure, *J. geophys. Res.*, **74**, 5949.

Hope, L. L., 1968. Brillouin scattering in birefringent media, *Phys. Rev.*, **166**, 883.

Horai, K., 1971. Thermal conductivity of rock-forming minerals, *J. geophys. Res.*, **76**, 1278.

Jordan, T. H. & Anderson, D. L., 1974. Elastic structures from free oscillations and travel times, *Geophys. J. R. astr. Soc.*, **36**, No. 2.

Klein, W. R. & Cook, B. D., 1967. Unified approach to ultrasonic light diffraction, *IEEE Trans. Sonics & Ultrasonics*, **SU–14**, 123.

Kumazawa, M., 1969. The elastic constants of polycrystalline rock and non-elastic behavior inherent to them, *J. geophys. Res.*, **74**, 5311.

Lewis, M. F., 1966. Elastic constants of magnesium aluminate spinel, *J. acoust. Soc. Am.*, **40**, 728.

McSkimin, H. J., 1961. Pulse superposition method for measuring ultrasonic wave velocities in solids, *J. acoust. Soc. Am.*, **33**, 12.

McSkimin, H. J. & Andreatch, P., 1962. Analysis of the pulse superposition method for measuring ultrasonic wave velocities as a function of temperature and pressure, *J. acoust. Soc. Am.*, **43**, 609.

Nye, J. F., 1957. *Physical properties of crystals*, p. 251, Oxford University Press, London.

O'Connell, R. J. & Graham, E. K., 1971. Equation of state of stoichiometric spinel to 10 kbar and 800 °K, *Trans. Am. geophys. Un.*, **52**, 359.

Papadakis, E. P., 1967. Ultrasonic phase velocity by the pulse-echo-overlap method incorporating diffraction phase corrections, *J. acoust. Soc. Am.*, **42**, 1045.

Rigby, G. R., Lovell, G. H. & Green, A. T., 1946. Some properties of the spinels associated with chrome ores, *Trans. Brit. ceram. Soc.*, **45**, 137.

Sammis, C. G., 1972. Lattice dynamics of MgO, Al_2MgO_4 and Mg_2SiO_4 spinel, *Geophys. J. R. astr. Soc.*, **29**, 15.

Schaefer, C. L. & Bergmann, L., 1934. Uber neue Beugungsercheinungen an schwingenden Kristallen, *Naturwiss.*, **22**, 685.

Sittig, E. K. & Cook, H. D., 1968. A method for preparing and bonding ultrasonic transducers used in high frequency digital delay lines, *Proc. IEEE*, **56**, 1375.

Spetzler, H., 1970. Equation of state of polycrystalline and single-crystal MgO to 8 kilobars and 800 °K, *J. geophys. Res.*, **75**, 2073.

Spetzler, H. A. & Anderson, D. L., 1971. Discrepancies in elastic constant data for MgO polycrystals and single crystals, *J. Am. Ceram. Soc.*, **54**, 520.

Stromberg, H. D. & Schock, R. N., 1970. A window configuartion for high pressure optical cells, *Rev. Sci. Instr.*, **41**, 1880.

Thomsen, L., 1972a. Elasticity of polycrystals and rocks, *J. geophys. Res.*, **77**, 315.

Thomsen, L., 1972b. On the effects of pressure upon rock elasticity, *Phys. Earth Planet. Int.*, **5**, 325.

Thurston, R. N., 1964. Wave propagation in fluids and normal solids, *Physical acoustics*, IA, 2–109, ed. W. P. Mason, Academic Press, New York.

Whittaker, E. T. & Robinson, G., 1944. *The calculus of observation*, Blackie, London.

Willard, G. W., 1949. Criteria for normal and abnormal ultrasonic light diffraction effects, *J. acoust. Soc. Am.*, **21**, 101.